DIPLOMA THESIS

Construction of a Scanning Force Microscope and Force-Distance Measurements on Gold and Graphite Surfaces

Peter Vorburger

under the guidance of
Dr. Thomas Ihn
Jörg Rychen

Prof. Dr. Klaus Ensslin

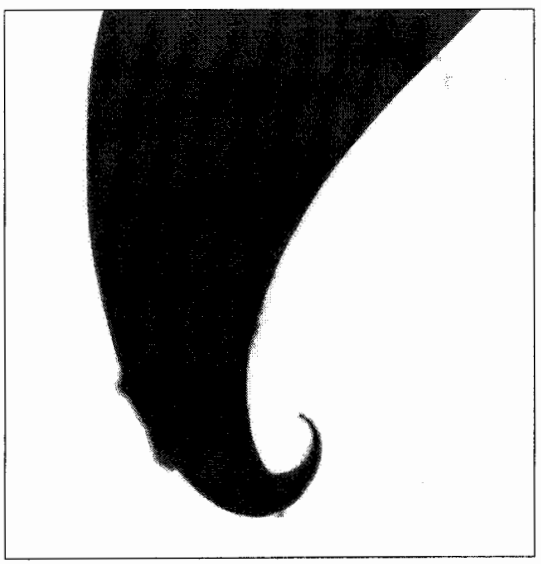

Laboratory of Solid State Physics
ETH Zürich

Summer Term 1999

The picture on the front page shows a tungsten tip that rolled up while etching. The picture shot by TEM is of the size $7.3\,\mu\text{m} \times 7.45\,\mu\text{m}$.

gewidmet meiner langjährigen Freundin

Sarah Altherr

Contents

1 Introduction

The aim of this diploma thesis was to set up and operate a dynamic scanning force microscope (SFM), followed by investigations on interaction forces between tip and sample.

Tuning forks are employed as sensor to detect the interaction force between tip and sample. The advantage of tuning forks are small oscillation amplitudes and a high spring constant which gives us the possibility to approach the surface without snapping into contact.

In part I the mechanical and electronical setup of the SFM is described and discussed. The result of this part is that the SFM really works.

The second part is focussed on tip preparation by electrochemical etching. We developed a production technique that allows us to manufacture reproducibly tips. We etched Tungsten and Platinum/Iridium wires. The tips are smaller than 50 nm in diameter and we achieved tips of 10 nm in diameter for Pt/Ir.

The third part shows distance dependent investigations on interaction forces between tip and sample. We did measurements with Platinum/Iridium tips on Gold films and measurements using Tungsten tips to investigate the properties of Graphite surfaces. It turned out that the dominating force is the attractive capillary force due to a water film coating all surfaces. We estimated the water film to be $7 - 8$ nm thick at room temperature and room pressure. Additionally the behavior of electrostatic forces between tip and sample was investigated by applying voltage between tip and sample.

In part IV topographic pictures of an antidot lattice are presented. The pictures show that structures of the size of about 20 nm can be clearly distinguished from each other.

And finally suggestions to improve the performance of the SFM followed by ideas for further applications of the SFM are listed in part V.

In the Appendix is attached an operation manual of the SFM including a check list.

Part I

The Scanning Force Microscope Setup

1 Mechanical Setup

In this section the mechanical setup of the SFM is presented. We are concerned with the parts of direct relevance to our measurements and the physics behind them. Details of the construction are listed in Ref.[1]. First a short overview is given. Then we focus on the problem of vibrations that limit the resolution of the measurements. In the following the setup to control the measurement environment, i.e. vacuum chamber and heater, is discussed and we finish with the positioning devices. In conclusion it must be mentioned that without the engagement of Andreas Herrmann this setup would not have be realized in time.

1.1 Overview

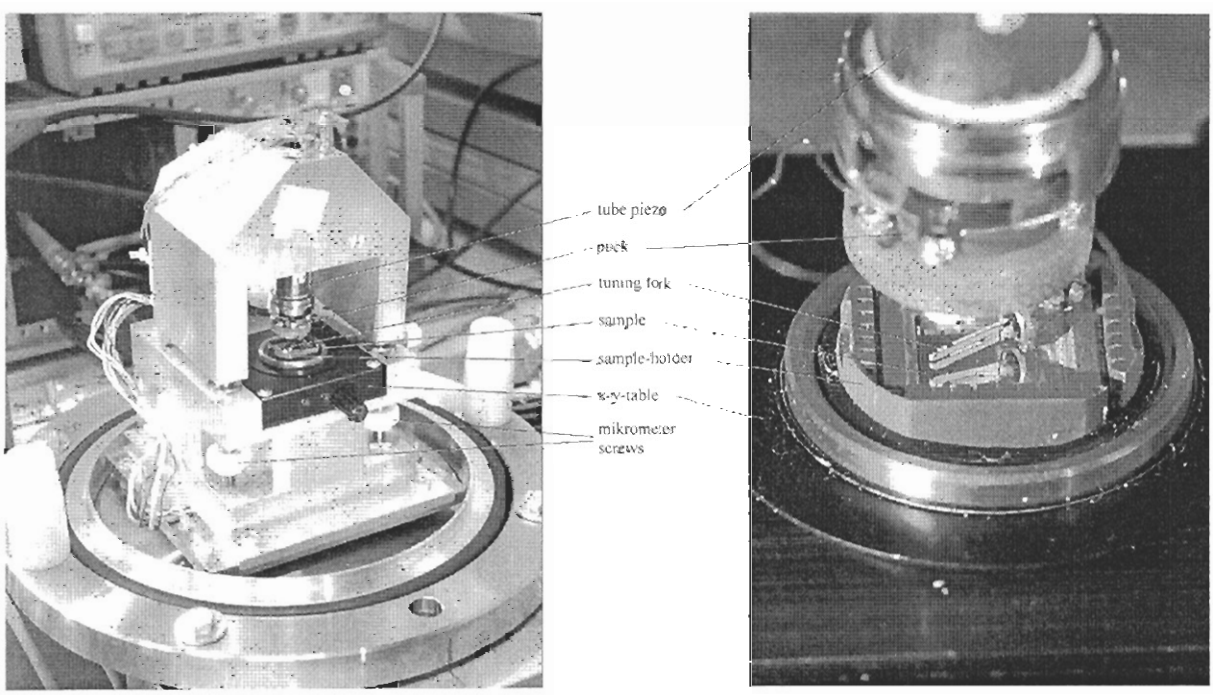

Figure 1: The picture on the left side shows an overview of the SFM and the picture on the right shows more details.

On the left picture in Fig.1 an overview of the SFM setup is shown. The SFM is placed in the center of the rubber ring where the vacuum chamber can be put on. On the right side of Fig.1 the same setup is shown, but zoomed in. It shows the tuning fork fixed by the fork holder that is screwed on the puck which is mounted at the end of the piezo

tube. The fork is fixed over a sample surface where the mirror image of the fork can be recognized. The individual parts of the SFM are marked in Fig.1 and described in the following sections in detail.

1.2 Vibration Isolation

Vibration isolation is crucial for SFM. Interfering signals add noise to the electronics and vibrations disturb the mechanical detection process, too. To avoid resonances we put the SFM on a huge mass that is elastically damped and we have to choose components of the SFM as stiff as possible.

1.2.1 Damped Table

To avoid vibrational disturbance of the measurement it is helpful to fix the SFM on a damped massive table. The design of our setup consists of an open box filled with sand standing on styrofoam as shown in Fig.2. A massive plate is put on the sand without any contact to the walls of the box. Obviously the electronics are not mounted on the same plate as the SFM, because the electronics are a source of vibrations, too. Nevertheless the driving mechanism has to be connected to the measuring unit without any transfer of vibrations. This is sufficiently solved by leading the wires through the sand.

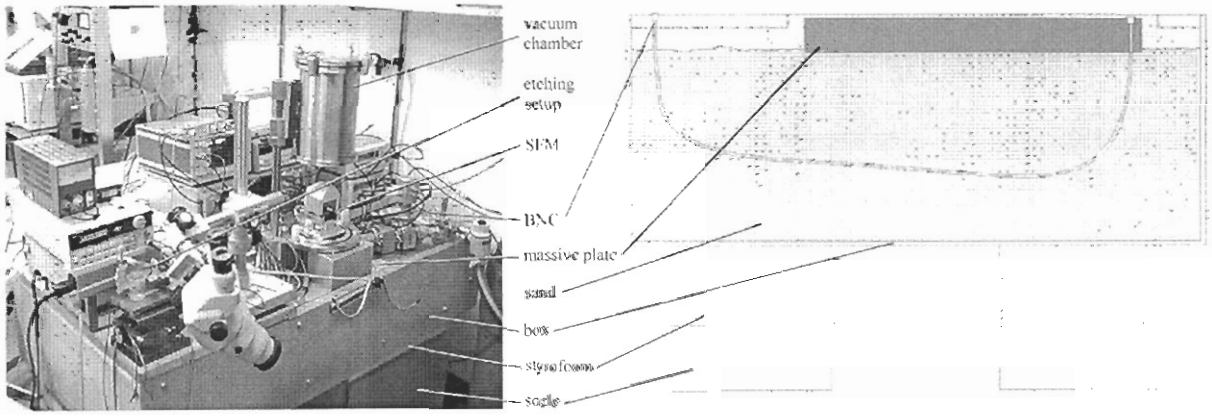

Figure 2: The picture on the left side shows the table with the SFM mounted on it and on the right side the corresponding schematic drawing is shown.

We compared different techniques of damping with our setup to determine the effectivity of our damping method. A first check is to stimulate resonances by knocking on the setup and detect resonances by ear. Our hearing is limited and therefore we employed a seismic detector[14] in combination with a frequency analyzer. The resonances of four different types of tables were investigated in a range from 0 Hz to 200 Hz. First, a common table with a Oxford magnet power supply on it, second, an air-damped table[1] of the manufacturer Newport, third, a setup that is suspended on rubber ropes without any contact to ground[2] and fourth, our sand- and styrofoam-damped table. The measurements of the common table in Fig.3a show huge noise in the whole range that gives reason enough for

[1]HPF C17, where the Topometrix Accurex AFM is mounted
[2]HPF C17, the low-temperature SFM built up by J. Rychen

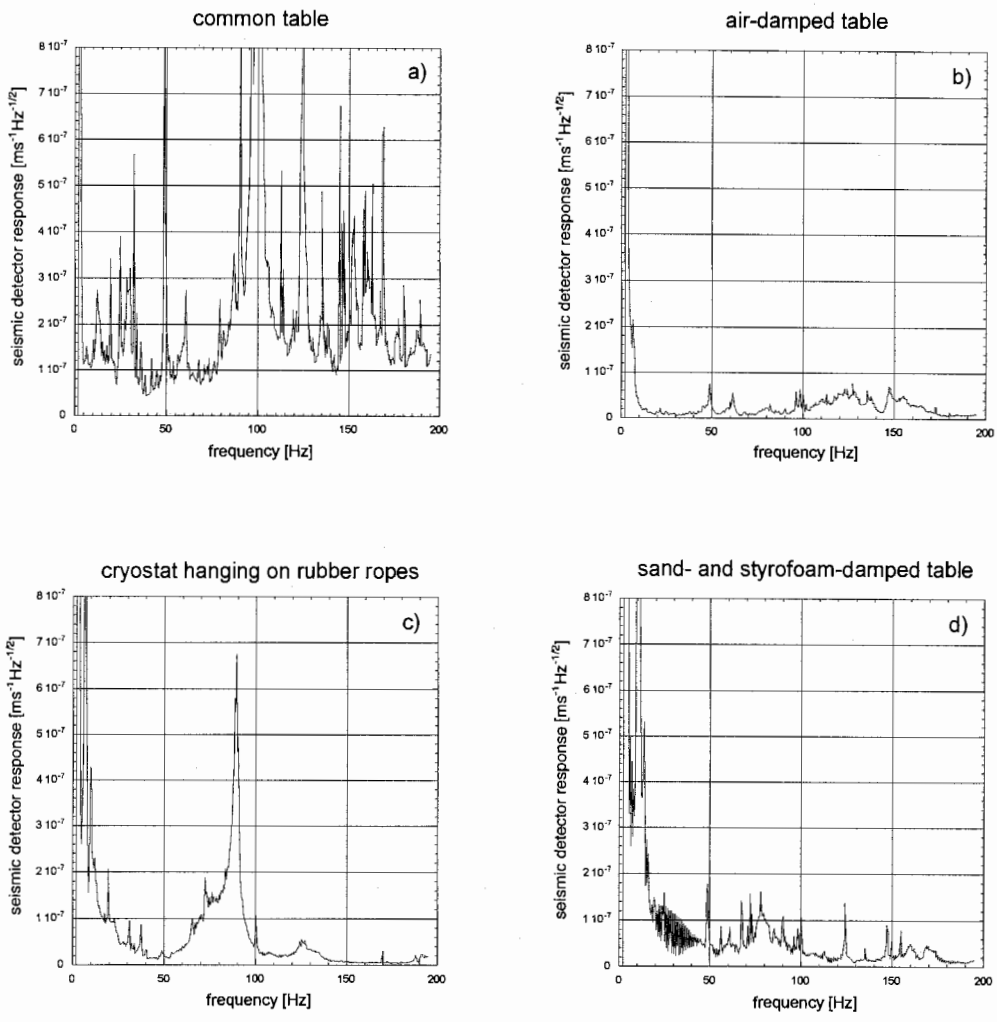

Figure 3: Seismic investigation on four different types of tables. a) a common table with an electronic compound on it. b) an air-damped table and c) a setup that is hung up on rubber ropes without any contact to ground. d) the sand- and styrofoam-damped table we used.

the use of a damped table to protect our sensitive machine from any vibrations. Fig.3b shows the resonances of the air-damped table that damps very effectively in the whole range, especially the damping in the low frequency region is favorable. The simple damping method of hanging up the setup on rubber ropes on the ceiling seems to be effective, but not satisfactory enough at very low frequencies as sketched in Fig.3c. The setup hanging on the ceiling consists of a cryostat where a SFM can be put in. The huge resonance around 90 Hz is due to the resonance frequency of the cryostat-chamber. The resonance characteristic of our table (Fig.3d) is comparable with those of Fig.3c with the difference of the absence of the resonance peak around 90 Hz and a less favorable behavior of the background noise in the whole frequency range. To conclude, the damping of our setup is not as effective as that of the air-damped table, but the characteristics of our table are comparable to those of the suspended setup without regard to the resonance peak at 90 Hz. With the setup c) of the SFM pictures of high resolution were achieved, therefore the damping of our SFM is sufficient.

1.2.2 Resonances of the Piezo Tube

The piezo tube is described in detail in section 1.4.2. We focus now only on the resonances of the tube. The tip of the SFM follows the shape of the surface while scanning. If there is a periodic structure on the surface the tip moves up and down. The moving of the tip can be considered as an oscillation with a frequency depending on the scanning velocity. To avoid resonances we have to set the velocity of the tip as slow such that no resonance of the system can be stimulated. The piezo tube is the component in touch with the puck (Fig.1) with the lowest resonance frequency. Therefore we are looking for the lowest resonance frequency of the piezo tube which we desire to be as high as possible because it limits the scanning velocity.

The lowest frequency is given by the bending mode for a long uniform rod, clamped at one end and free at the other end[2]

$$f = \frac{0.56\kappa c}{L^2}, \tag{1}$$

where $c = (Y/\rho)^{1/2}$ is the velocity of sound, Y is Young's modulus, ρ is the density of the material, L is the length, and κ is the radius of gyration about the neutral axis of the cross section and is for a tube

$$\kappa = \frac{1}{8}\sqrt{D^2 + d^2}, \tag{2}$$

where D and d are the outer and inner diameters, respectively.

Using the characteristic data[13] of the tube

Outer Diameter	$D = 0.5\,\text{in} = 12.7\,\text{mm}$
Wall Thickness	$D - d = 0.02\,\text{in} = 0.51\,\text{mm}$
$\Longrightarrow$ Inner Diameter	$d = 0.48\,\text{in} = 12.19\,\text{mm}$
Length	$L = 2\,\text{in} = 50.8\,\text{mm}$
Piezoelectric Constant d_{31}at 20 °C	$d_{31} = -2.62\,\text{Å}\,/\,\text{V}$
Piezoelectric Constant d_{33}at 20 °C	$d_{33} = 5.83\,\text{Å}\,/\,\text{V}$
Youngs Modulus	$Y = 6.3 \cdot 10^{10}\,\text{N}\,/\,\text{m}^2$
Thermal Expansion Coefficient	$\alpha = 4,7\text{ppm}/\,°\text{C}$
Mass	$m_{\text{piezo}} = 6.95$ g

the resonance frequency of the bending mode is

$$f = 1388.7\,\text{Hz} \tag{3}$$

The resonances are measured with the setup shown in Fig.4. Compared to the theoretical result (3), the measurement of the resonance peak (Fig.5) shows a huge frequency shift of the resonance peak downwards to 650 Hz with a less pronounced peak at 680 Hz. An explanation for this shift is the additional mass fixed at the end of the tube. Therefore we have to refine the computation.

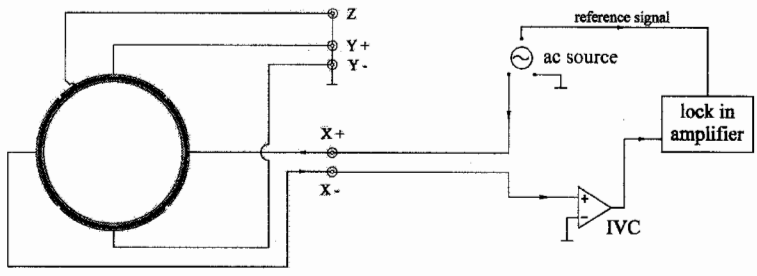

Figure 4: Setup for the measurement of the resonances of the piezo tube. The tube is connected with one outer electrode to a frequency generator and the outer electrode on the opposite side is connected to a lock in amplifier. The remaining electrodes are grounded. The tube is stimulated by an ac voltage at a certain frequency and the lock in amplifier measures the current generated by the movement of the piezo tube.

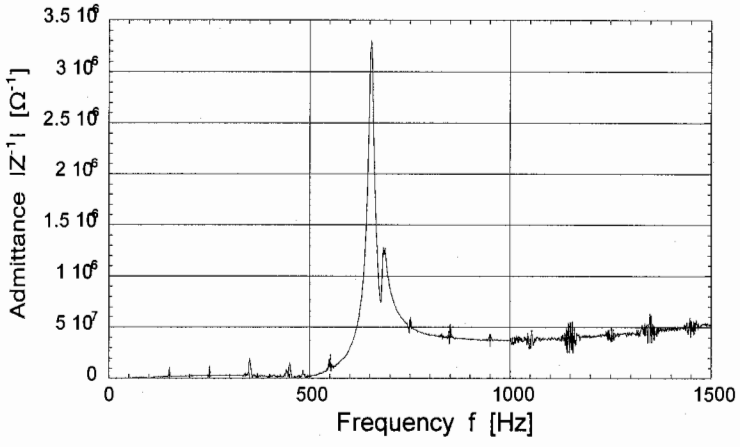

Figure 5: Lowest resonance peak of the piezo tube. The peak corresponds to the bending mode.

Under the assumption that the oscillation of the end of the tube is harmonic with small amplitude, the movement can be described by a spring pendulum. A pendulum obeys the equation of motion

$$\frac{d^2}{dt^2}x\left(t\right)+\omega^2 x\left(t\right)=0, \tag{4}$$

where $\omega^2 = k/m$, k denotes the spring constant and m the mass of the oscillating object. First we look at the piezo without any mass added. Because of the special geometry of the tube and the type of oscillation, an effective mass $m^{\text{eff}}_{\text{piezo}}$ different to the measured mass of the piezo $m_{\text{piezo}} = 6.95$ g is expected. The spring constant is given by[2]

$$k=\frac{3YI}{L^3}, \tag{5}$$

where $I = \frac{\pi}{64}\left(D^4 - d^4\right)$ is the moment of inertia of a tube. Thus using the angular velocity $\omega = 2\pi f = 2\pi \cdot 1388.7\,\text{Hz}$ we obtain

$$m^{\text{eff}}_{\text{piezo}}=\frac{k}{\omega^2}=\frac{1}{\left(2\pi f\right)^2}\frac{3Y}{L^3}\frac{\pi}{64}\left(D^4-d^4\right)=3.64\,\text{g}=0.52\cdot m_{\text{piezo}} \tag{6}$$

Now we fix an additional mass M at the lower end of the piezo. The total mass is now $m_{\text{tot}} = M + m_{\text{piezo}}^{\text{eff}}$ because mass adds linear in the kinetic energy. The additional weight of the puck holder, puck, fork holder and fork (Fig.1) together is $M = 4.7\,\text{g}$. Under the assumption that the spring constant does not change the modified resonance frequency is

$$\omega_{\text{modified}} = \omega \cdot \sqrt{\frac{m_{\text{piezo}}^{\text{eff}}}{m_{\text{tot}}}} = \omega \cdot \sqrt{\frac{1}{1 + \frac{M}{m_{\text{piezo}}^{\text{eff}}}}} = 917.4\,\text{Hz}\,. \tag{7}$$

A massive frequency shift of 471.3 Hz downwards, but not big enough compared with the measurement in Fig.5. A correction downwards can be explained by recognizing that the additional mass is mounted *at* the very end of the tube, i.e. the effective mass of the puck has to be corrected to be bigger than M.

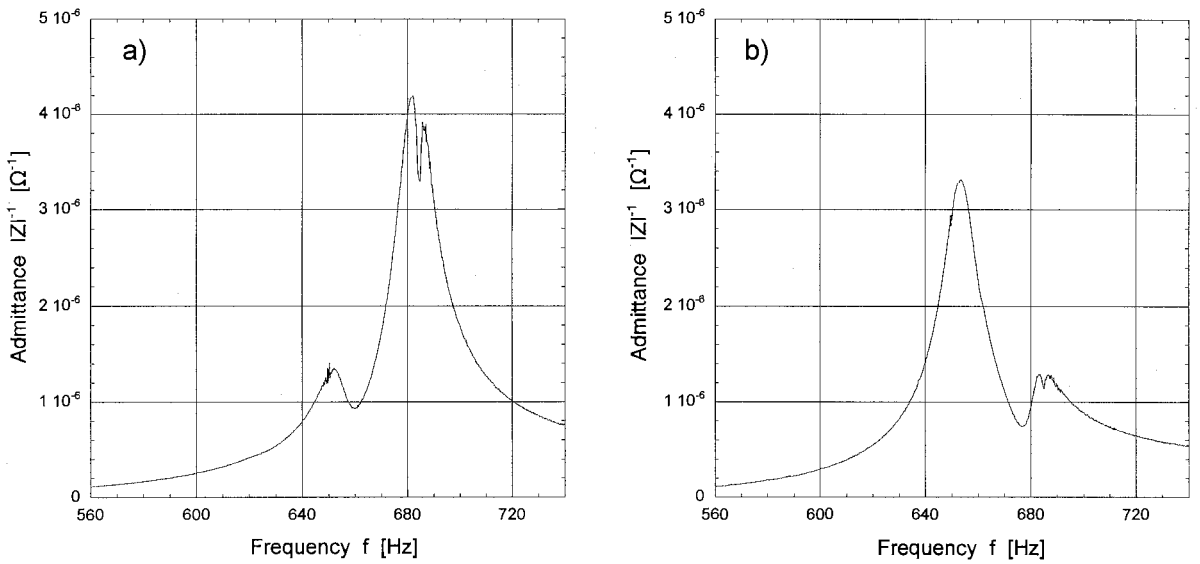

Figure 6: Admittance of the piezo tube at the resonance frequency of the bending mode. The graph on the left side shows the bending along the x-axis and the graph on the right shows the perpendicular bending along the y-axis.

Fig.6a and Fig.6b show the resonance peak of the bending mode of the piezo in x- and y-direction, respectively. Fig.6a shows a huge peak with two maxima at 684 Hz and 688 Hz and a less pronounced peak at 653 Hz. In Fig.6b the situation is contrary: the huge resonance is placed at 653 Hz and the smaller one with two maxima at 684 Hz and 688 Hz. Comparison of the two plots in Fig.6 shows that there are two different resonance frequencies in x and y direction and they do crosstalk. In a totally symmetric system the two resonance frequencies should be identical. But in reality the puck itself is not symmetric and it is not placed exactly in the center of the tube.

1.3 Vacuum Chamber and Heater

All surfaces are covered with a thin water film as long as they are not hydrophobic. It is desirable to have no such film on the sample in SFM because it changes the character and behavior of the interaction between tip and sample. The screening of the interaction by the water film disturbs pure force-distance measurements between tip and substrate . A way to get rid of this film is to heat the substrate and to pump away the damp, therefore a UHV chamber (10^{-11} mbar) is optimal.

The vacuum chamber employed is made of a simple pot put over the scanning unit of the SFM. Pressures of about 10^{-4} mbar were achieved with this setup, not comparable with UHV. Hence, we are not able to make the water film totally vanish, but we have the additional effect that the Q-factor of the tuning fork increases, because there is less air left to damp the fork (Fig.16 on page 19). The quality of our vacuum chamber is mainly limited by the creeping of the gas out of the space between screws and screwholes and the space between the screwed components, respectively.

The heater is placed below the chip-carrier. The heating unit consists of a konstantan wire and a platinum resistance Pt1000 is used as temperature detector. The resistance of Pt1000[17] is $1000\,\Omega$ at $0\,^{\circ}\mathrm{C}$ and the temperature dependence of the resistance in the range from $0\,^{\circ}\mathrm{C}$ to $850\,^{\circ}\mathrm{C}$ is $R_{\mathrm{Pt1000}} = 1000\,\Omega \cdot (1 + 3.90802 \cdot 10^{-3} \cdot T - 0.5802 \cdot 10^{-6} \cdot T^2)$, where T denotes the temperature in $^{\circ}\mathrm{C}$. The sample is thermally coupled to the heating unit by a copper link. The heater is driven by a two-point regulator. Usually the sample is heated for several hours at a temperature between 110 to $120\,^{\circ}\mathrm{C}$.

1.4 Positioning Devices

The function of the positioning devices is to place the tip over the region of interest and to control the tip-sample distance.

1.4.1 x-y-Translation Table with Sample Holder

The sample is placed by the x-y-translation table under the tip. The positioning is done by micrometer screws. The accuracy of the screws is $317.5\,\mu\mathrm{m}$/turn. This is precise enough to follow a hall bar using a scanning range of the SFM of $15\,\mu\mathrm{m} \times 15\,\mu\mathrm{m}$.

A chip socket is mounted on the x-y-table. The sample is mounted on a chip-carrier and can be connected to the socket by 12 contacts as sketched in Fig.7.

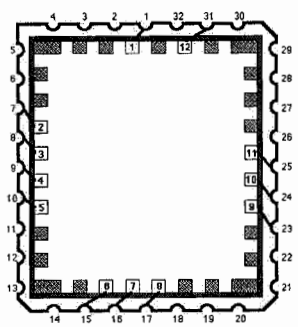

Figure 7: Illustration of the chip carrier. The sample can be connected to 12 contacts. The positions of the contacts are labelled.

1.4.2 Piezo Tube

The piezoelectric effect was discovered by Pierre and Jacques Curie (1880) [2]. They sandwiched a long, thin quartz plate between two tin foils. While one tin foil was grounded, the other tin foil was connected to an electrometer. By applying a longitudinal tension on the plate, an electrical charge was detected by the electrometer.

After the prediction of an inverse piezoelectric effect by Lippmann (1881) the Curie Brothers verified that by applying a voltage to the tin foils, the quartz plate elongated or contracted depending on the polarity of the applied voltage.

We use the inverse piezoelectric effect to position the tip on the sample surface. A tube-shaped piezo with an electrode inside and four electrodes at the outside (Fig.8) is employed to vary the tip-sample distance and to carry out the x-y-scanning movements. The tip-sample distance is regulated by applying a voltage between the inner and outer electrodes. Applying voltages asymmetrically at two opposite outer electrodes causes a bending of the tube, i.e. a lateral movement of the lower end due to elongation and contraction of the material at opposite sides.

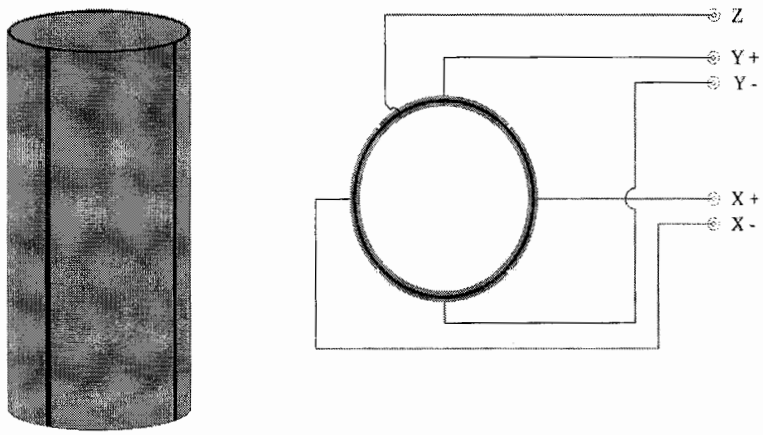

Figure 8: Side-view and vertical projection of a piezo tube. The electrodes and contacts are shown on the vertical projection on the right side.

The piezo is driven by five high-voltage amplifiers, one for each single electrode on the tube. According to the data sheet[13] the maximal voltage range of the tube is $\pm 215\,\mathrm{V}$ for movements in the lateral x-y-plane and $\pm 75\,\mathrm{V}$ along the z-axis, therefore a maximal working range of the potential difference of $\pm 70\,\mathrm{V}$ in every direction was chosen. In the case of maximal elongation and maximal bending of the tube the maximal potential difference of $140\,\mathrm{V}$ between the inner and one outer electrode can be reached. The $140\,\mathrm{V}$ potential difference is within the tolerance. Using the calibration data from the data sheet

movement in z-direction per applied voltage difference:	$337\,\text{Å}\,/\,\mathrm{V}$
movement in x–y-direction per applied voltage difference:	$1214\,\text{Å}\,/\,\mathrm{V}$

it turns out that the maximal z-range is $\pm 2,361\,\mu\mathrm{m}$ corresponding to $\pm 70\,\mathrm{V}$ and the deflection in the x or y direction is $\pm 8,425\,\mu\mathrm{m}$.

A serious problem of the piezoelectric material is thermal expansion (thermal expansion coefficient $\alpha = 4,7\mathrm{ppm}/\,^{\circ}\mathrm{C}$). It follows that the expansion of the tube employed is

about 235 nm / °C in z-direction, i.e. a temperature increase of 20 °C causes an expansion of 4.7 μm. The distance of 4.7 μm exceeds the maximal z-range of the piezo tube! While heating the sample (section 1.3), the piezo gets warm and as observed in most cases the tip drives into the sample.

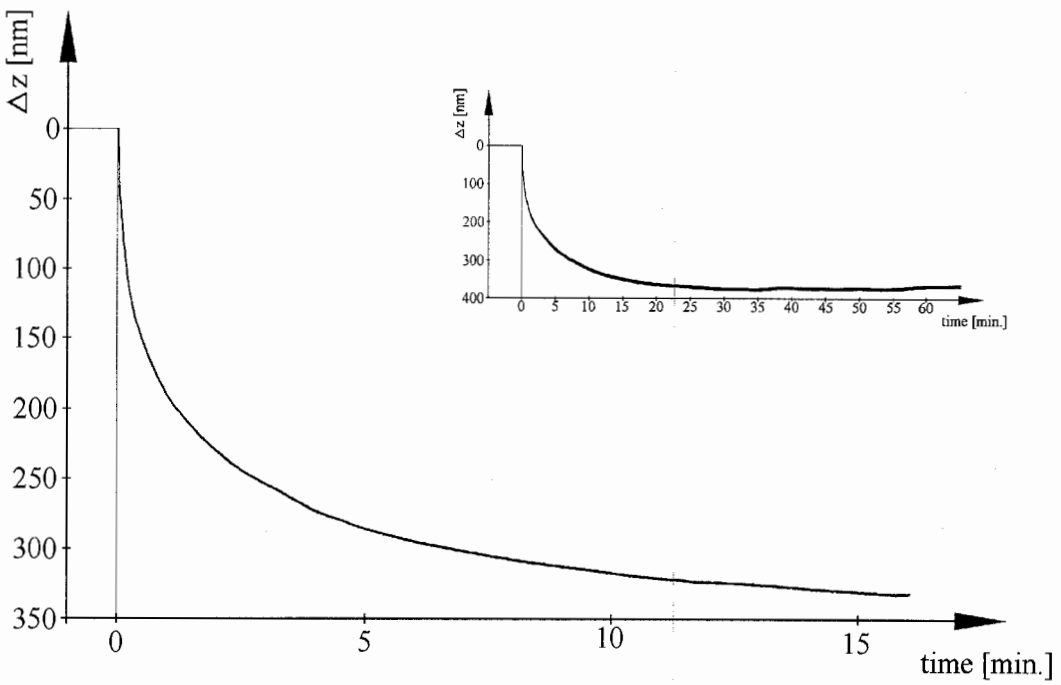

Figure 9: Creep of the piezo tube. The shape of the curve indicates logarithmic decay in time. The inset shows the process on a larger time scale: after 30 min the creep is negligibly small.

Another disadvantageous property of the piezoelectric material is hysteretic behavior. The piezo tube elongates or contracts if a voltage is applied to the piezo, but the tube does not stop at the desired position. It continues with the elongation or contraction. This hysteretic behavior is called piezo creep. We measured the additional elongation indirectly by approaching the tip to the sample and enabling the z-feedback (section 2.3). The z-feedback loop keeps the tip at a fixed distance over a point of the surface by controlling the voltage applied on the piezo. If the tube material itself elongates, the z-feedback has to decrease the applied voltage to keep the tip-sample distance constant. By recording the voltage input to the piezo tube the effective elongation of the tube can be calculated. Fig.9 shows the additional elongation of the piezo tube versus time. The tip was withdrawn for 45 min, after that the tip was approached and at time $t = 0$ s the z-feedback loop locked. Fig.9 shows that the additional elongation of the piezo material decays logarithmically in time. The total elongation depends on temperature and on the voltage difference that was applied before reaching the point of measurement. In our example the temperature was 300 K and the applied voltage was initially -70 V and the z-feedback was enabled at $+17.5$ V. The inset in Fig.9 tells us that at 300 K we have to wait about 30 min until the creep has a negligeable influence to the measurements. The inset shows a total additional elongation of 360 nm which is a huge distance compared to the scale of nanometers we are dealing with.

1.4.3 Coarse Approach

The coarse approach is done with micrometer screws. As sketched in Fig.1 the mounting of the piezo tube and the scanning unit rests on three micrometer screws, two in the front, one in the rear. The two in the front are employed for the coarse approach, observed by microscope. The approach by screwing the third is more precisely due to the leverage, because the tip is placed about five times closer to the screws in the front than to the screw in the rear.

2 Electronic Setup

In this section the electronic setup of the SFM is presented. First a short overview is given. Then we motivate the use of a phase locked loop (PLL) and we show how it is realized in our SFM. In section 2.3 the z-feedback loop is discussed. In conclusion it must be mentioned that without the engagement of Paul Studerus this SFM could not have been realized in time.

2.1 Overview

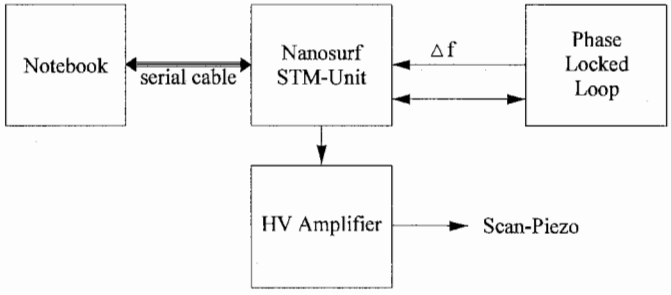

Figure 10: Schematic setup of the electronics.

The electronic setup is based on a Nanosurf[15] STM setup and is controlled by a modified Nanosurf software. The schematic setup is shown in Fig.10. The main function of the electronics is first to detect any force acting on the tip, second to keep the force constant while scanning by regulating the tip-sample distance, or third to detect the force while changing the tip-sample distance.

2.2 Phase-Locked Loop

The purpose of the PLL is to stimulate the tuning fork on its resonance frequency and to follow immediately with the stimulation frequency if the resonance of the fork varies. The setup of the phase locked loop (PLL) is schematically drawn in Fig.11 and its components are explained in the following sections. The setup is divided into two parts, the "Nanosurf" electronics working with voltage of 10VPP and the part including the tuning fork working in the range of millivolts shown as dashed region in Fig.11.

The interacting force between sample and tip acts on the tuning fork and shifts its resonance frequency. In principle it is sufficient to hold the tip over the sample surface and to detect the frequency shift. But the quality-factor of a brand new fork in vacuum is about 50000 and the resonance frequency of interest is 32768 Hz . That means that the adaptation of the fork to a new frequency is of the order of seconds, much to slow for practical use.

The solution to accelerate the adaptation of the fork to the shifted frequency is to detect the frequency shift in the very beginning followed by a stimulation of the fork at the shifted frequency. Very helpful is the fact that the phase of the fork flips with a very steep slope at its resonance as shown in Fig.15 on page 18. This feature of the phase flip is used to detect any change of the resonance frequency as plotted in Fig.12. In Fig.12a we

focus on a point in the middle of the phase branch with negative slope. The slope of the phase jump is so steep that a small shift of the frequency causes a huge movement along the phase branch. For example in Fig.12b a frequency shift of 1 Hz occurs and causes a phase shift of almost 50 °. The phase shift can be balanced out by stimulating the fork at the new, shifted frequency (Fig.12c). Implementing this process in a loop makes the fork reacting very fast on any force acting on it. Because we are locking the loop on the phase, the loop is called "phase locked loop".

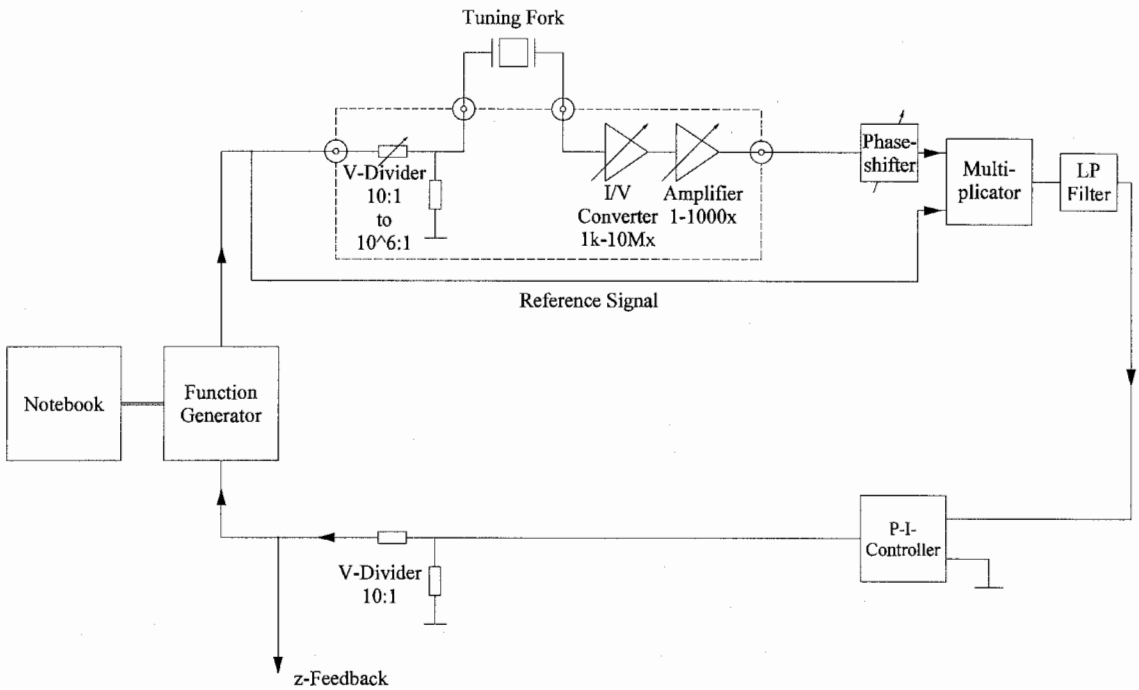

Figure 11: Circuit diagram of the PLL.

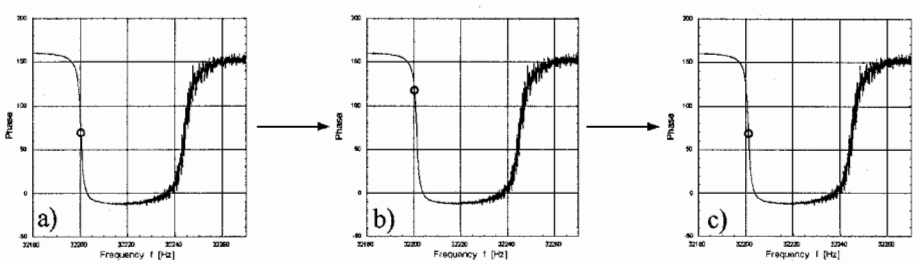

Figure 12: Illustration of the function of the PLL. First, a marked point is placed on the negative slope of the phase jump on the actual stimulation frequency of the fork. On the second plot the resonance of the fork is shifted 1 Hz and causes a shift of the phase of 50 °. This phase-shift is detected by the PLL and the stimulation of the fork is raised to the new resonance frequency. In the third plot the marked point is again placed on the negative slope of the phase jump and on the actual resonance frequency of the fork.

2.2.1 Tuning Fork

The tuning fork is our probe to detect any force acting on the tip of the SFM. Tuning forks are very stable oscillators. Due to their use in industry they are very cheap and easily available. The characteristic data[9] of the employed tuning fork are

piezoelectric constant d_{11} at 20 °C	2.31 pm / V
piezoelectric constant d_{14} at 20 °C	−0.727 pm / V
length of an arm of the fork L	3.7 mm ±0.02 mm
width of an arm b	0.45 mm ±0.02 mm
height of an arm h	0.25 mm ±0.02 mm
density ρ	2659 kg / m^3
Youngs modulus Y	$7.87 \cdot 10^{10}$ N / m^2

The tuning fork is made of α-quartz, a piezoelectric material, and is stimulated[9] by applying ac voltage on its resonance frequency. The stimulation voltage amplitude of the fork is of the order of mV and therefore the output voltage of 10VPP of the "Nanosurf" frequency generator is divided as shown in Fig.11. The dividing factor can be set from 10 to 10^6. The output current of the stimulated fork is first converted to voltage and then multiplied until the signal is of the order of 10VPP, the working range of the remaining "Nanosurf"electronics. The amplitude of the fork can be determined by measuring the output current and applying the transformation factor 0.71 nm / nA[8]. The signal is amplified in two steps, first by the I/V-Converter with a factor of 10^3 to 10^7 and followed by a multiplicator of the factor from 1 to 10^3.

The resonance frequency of the tuning fork in the symmetric bending mode in the plane of the two arms is 32768 Hz = 2^{15} Hz and the Q-factor in vacuum is about 50000.

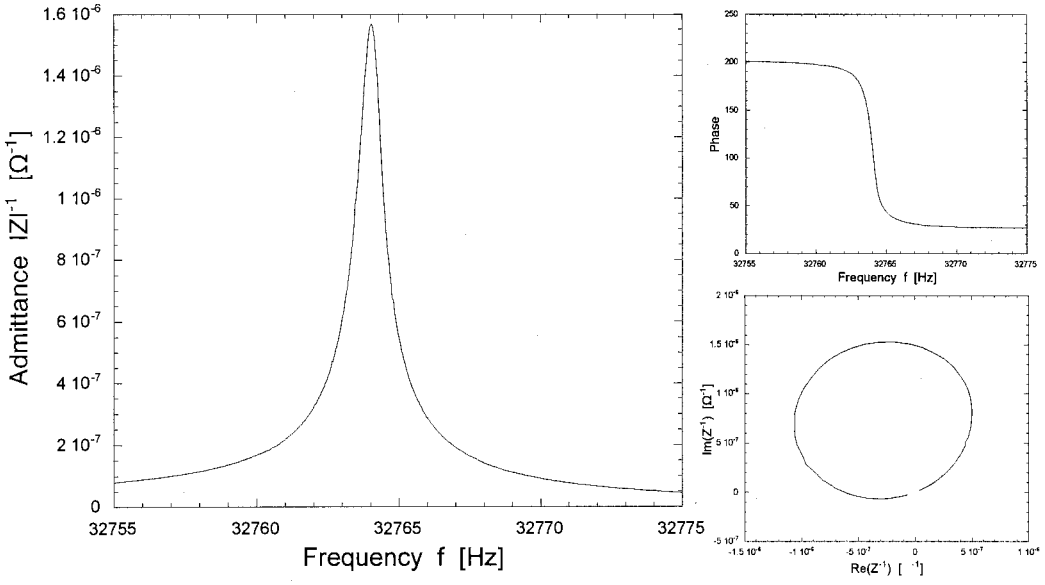

Figure 13: Resonance of an unprocessed tuning fork. The enclosing capsule has not been removed. The sharp resonance peak on the left plot and the phase jump on the right plot occur at 32764 Hz ≈ 2^{15} Hz .

Fig.13 shows the resonance of a unprocessed fork, measured by stimulating the fork with an ac-voltage and detecting the output current by a "lock in amplifier". The plot on the left in Fig.13 shows the absolute value of the admittance and the upper inset on the right side shows the phase versus frequency. On the lower inset on the right side the absolute value of the admittance and the appropriate phase are plotted in the complex plane. The capsule surrounding the tuning fork has not been taken off, therefore the measurement corresponds to a measurement of a fork in vacuum. The absolute value of the admittance shows at a first glance a Lorentz-like resonance at 32764 Hz, 4 Hz lower than the expected value of 2^{15} Hz. This deviation can be explained by ageing of the piezoelectric material. The quality factor of this fork is 44882 Hz.

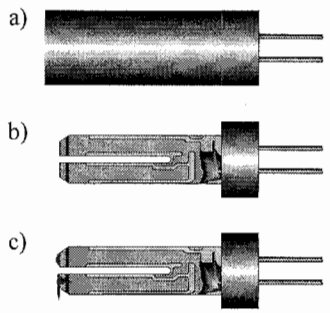

Figure 14: The preparation process of a tuning fork. a) shows the brand new fork enclosed in a capsule and b) shows the fork without capsule. In c) a tip is attached on the lower arm and a drop of glue of approximately the same weight is fixed on the upper arm to balance out the lower weight.

Before we can use the fork as detector in SFM we have to process it. First we remove the capsule that is enclosing the fork as drawn in Fig.14, step a) to b). Then a wire is fixed on the end of the lower arm with silver-epoxy glue[16] as shown in Fig.14c. The silver-epoxy glue is conducting. To balance out the weight on the one arm a drop of approximately the same weight is glued on the other arm. To gauge the tuning fork the producer cuts the metal layer on the end of the arms by a laser. This causes a loss of weight and a shift of the resonance upwards. Sometimes the gauging process cuts the electrical connection between tip and electrode. We bypass the intersection with silver-epoxy glue, because we want to connect the tip to a well defined potential.

Attaching weight on the arms of the fork changes its properties. Fig.15 shows the resonance of a tuning fork with additional weight on its arms, measured in vacuum of $4.5 \cdot 10^{-4}$ mbar. The centerfrequency of the resonance is shifted 567.5 Hz downwards to 32200.5 Hz. The amplitude of the absolute value of the admittance is 80% lower compared to the pure fork in Fig.13. The quality factor decreased to $Q = 18620$ corresponding to 41% of the original value. The phase plotted in Fig.15 shows an additional phase jump at 32243 Hz indicating that the simple model of an Lorentz-oscillator has to be modified. In Ref.[18] and [19] a model of an equivalent circuit is proposed that is able to explain the resonances in Fig.15.

The properties of the tuning fork depend also on the surrounding medium. In Fig.16 the same tuning fork was investigated as in Fig.15. The measurement shows the resonance of the fork in vacuum and at atmospheric pressure. Additionally the resonance of the fork was investigated in He-gas at atmospheric pressure. Below the obtained quantities that

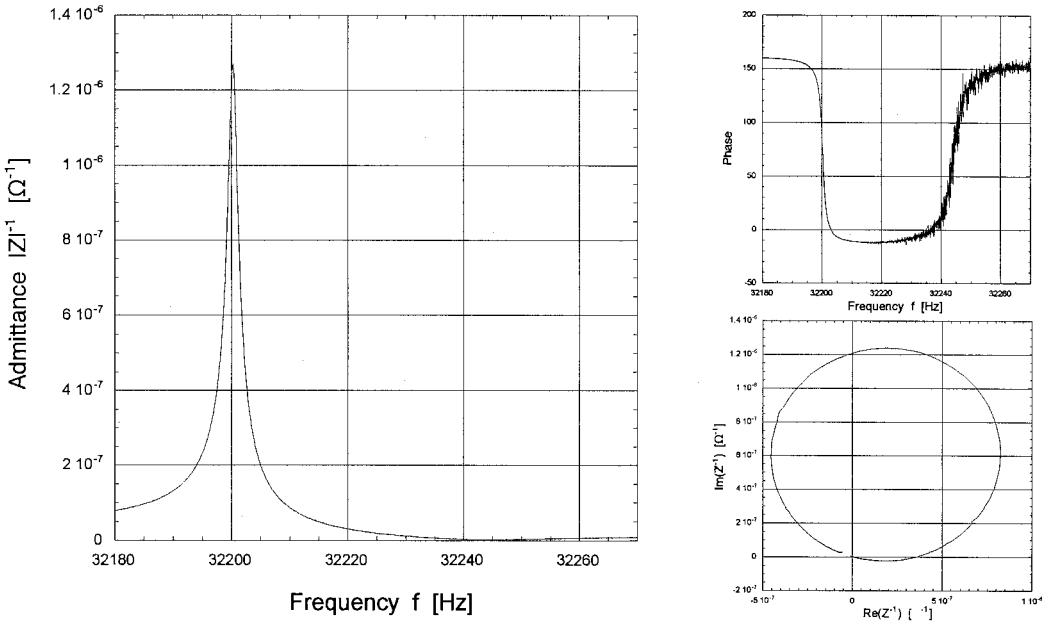

Figure 15: Resonance peak of a tuning fork in vacuum with additional mass on its arms. The center frequency of the resonance is at 32201 Hz.

characterize the system are listed:

medium, pressure	resonance frequency	resonance amplitude	quality factor Q
air, $4.5 \cdot 10^{-4}$ mbar	32200.5 Hz	$1.27 \cdot 10^{-6}\,\Omega^{-1}$	18620
air, 1 bar	32193.5 Hz	$5.4 \cdot 10^{-7}\,\Omega^{-1}$	8093
He,1 bar	32199 Hz	$8.2 \cdot 10^{-7}\,\Omega^{-1}$	12254

Compared to the resonance of the fork in vacuum the resonance in air at 1 bar is shifted 7 Hz downwards. The amplitude of the admittance at resonance is 42% and the quality factor is 43% of the vacuum value. This behavior can be explained by the following consideration. Increasing the pressure corresponds to an increase of the density of particles. The shift in frequency, the decrease in amplitude and the lowering of the quality factor can be explained because the oscillating fork is surrounded by more particles that increase the effective mass of the arms and damp the oscillation of the fork.

The resonance of the fork surrounded by He-gas at atmospheric pressure is shifted 1.5 Hz to 32199 Hz . The amplitude of the admittance at resonance is 65% and the quality factor is 66% of the vacuum value. The argument for the change of the characteristics are the same as above. But the changes are not as drastically as observed in air at 1 bar . The explanation is that perfect gas needs always the same molar volume. Air consisting mainly of nitrogen molecules N_2 can be assumed to be a perfect gas as well as helium He. Because the volume in the vacuum chamber does not change, the number of particles does not change either. That means that the fork is surrounded by the same number of particles in air and in helium, but N_2 is seven times heavier than He. Hence the effective mass of a fork arm in air is increased more in nitrogen than in helium and therefore the observed change in the characteristics is reasonable.

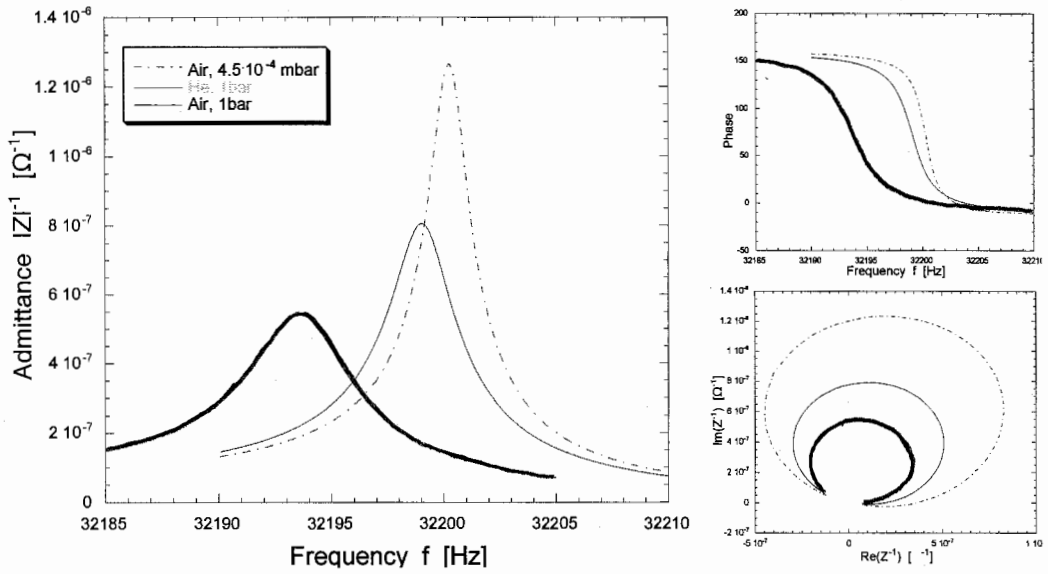

Figure 16: Resonance peaks of a tuning fork with additional mass on its arms in different environments and pressures.

Model of Two Coupled Pendula

The oscillation in the plane of the two arms of the tuning fork can be represented by the model of two coupled pendula. Under the assumption that both arms are of the same weight[3] the equations of motion [20] are

$$\begin{aligned} m_{\text{eff}}\ddot{x}_1 + k_{\text{a}}x_1 + \tfrac{1}{2}k_{\text{c}}\,(x_1 - x_2) &= 0 \\ m_{\text{eff}}\ddot{x}_2 + k_{\text{a}}x_2 + \tfrac{1}{2}k_{\text{c}}\,(x_2 - x_1) &= 0, \end{aligned} \tag{8}$$

where k_{a} is the spring constant of a single arm and k_{c} is the coupling between the two arms. The damping is not taken into account, because of its compensation by the driving mechanism. The oscillation of a single arm corresponds to the bending mode of a bar in the plane of the two arms and k_{a} is[2]

$$k_{\text{a}} = \frac{3YI}{L^3} = 8850\,\text{N}\,/\,\text{m} \pm 1380\,\text{N}\,/\,\text{m}, \tag{9}$$

using the moment of inertia $I = \frac{1}{12}hb^3$ of a bar. The deviation is influenced by the uncertainty of the dimensions of the fork arm. Therefore we treat now the calculations as estimations. Additionally the resonance frequency f_{a} of the bending mode of a single arm can be estimated by

$$f_{\text{a}} = \frac{0.56\kappa c}{L^2} = 28900\,\text{Hz} \pm 1300\,\text{Hz}, \tag{10}$$

[3]In part III, section 2.1 the model of the coupled pendula is treated more refined by taking into consideration that the arms of the tuning fork are of different weights.

using $\kappa = b/\sqrt{12}$, where b is the thickness of the bar in the plane of vibration and $c = \sqrt{Y/\rho}$ the velocity of sound. From Eq.9 and Eq.10 follows the effective mass of a single arm

$$m_{\text{eff}} = \frac{k_{\text{a}}}{(2\pi f_{\text{a}})^2} = 0.268\,\text{mg} \pm 0.048\,\text{mg} = (0.24 \pm 0.05)\, m_{\text{real}} \tag{11}$$

using the real mass $m_{\text{real}} = Lbh\rho = 1.1\,\text{mg} \pm 0.1\,\text{mg}$.

Diagonalizing Eq.8 yields two equations of the structure of a harmonic oscillator

$$\begin{aligned} m_{\text{eff}}\ddot{q}_1 + kq_1 &= 0 \\ m_{\text{eff}}\ddot{q}_2 + k_{\text{a}}q_2 &= 0, \end{aligned} \tag{12}$$

where $q_1 \equiv (x_1 - x_2)/\sqrt{2}$, $q_2 \equiv (x_1 + x_2)/\sqrt{2}$ and $k \equiv k_{\text{a}} + k_{\text{c}}$. The upper equation in

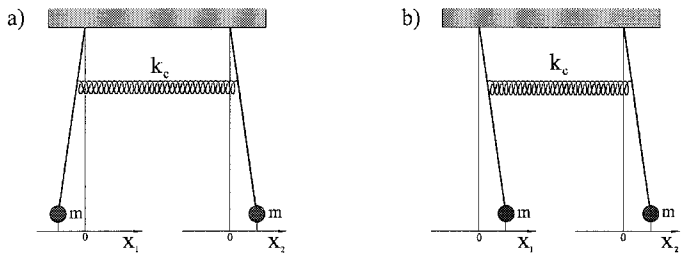

Figure 17: Schematic plot of two coupled pendula, where k_{c} denotes the coupling constant and x_1 the deflection of the first and x_2 the deflection of the second arm. a) shows the asymmetric and b) shows the symmetric mode of the system.

Eq.12 is the asymmetric and the lower equation is the symmetric mode of two coupled pendula as sketched in Fig.17. The symmetric mode oscillates with the same frequency like two free pendula, i.e. the pendula feel no coupling in this Eigenmode. The asymmetric mode shows an Eigenfrequency $\omega_0^2 = k/m_{\text{eff}} = (k_{\text{a}} + k_{\text{c}})/m_{\text{eff}}$. Comparing the two modes in Fig.17 shows that in the asymmetric mode the center of mass is fixed and in the symmetric mode the center of mass oscillates. The consequence is that the quality factor of the asymmetric mode is higher than that of the symmetric mode. Therefore we work on the resonance of the asymmetric mode of the tuning fork.

The estimation yields $k = m_{\text{eff}}\omega_0^2 = m_{\text{eff}}(2\pi f_0)^2 = 11400\,\text{N/m} \pm 2000\,\text{N/m}$. Knowing that the resonance frequency is $f_0 = 2^{15} = \omega_0/2\pi$ it turns out that the coupling constant is $k_{\text{c}} = 2510\,\text{N/m} \pm 2460\,\text{N/m}$. Although the deviation is of the order of the result we can conclude that k_{c} is smaller than the spring constant of one single arm k_{a}.

2.2.2 Phase Shifter, Multiplier and Filter

The phase shifter is placed between the amplifier of the output current of the tuning fork and the multiplicator as sketched in Fig.11. First the phase shifter helps to gauge the electronics by cancelling out improper frequency shifts due to voltage divider, I/V-converter and voltage amplifier. This gauge is carried out by comparing the phase-difference between the input signal of the voltage divider and the voltage output of the amplifier. Second it shifts the phase by 90 ° to prepare the signal for the multiplier.

The heart of the PLL is the multiplier. The multiplier multiplies the fork signal $U_f = \widetilde{U_f} \sin\left(\omega_f t + \varphi_f + 90\,^\circ\right) = \widetilde{U_f} \cos\left(\omega_f t + \varphi_f\right)$ with the reference signal $U_r = \widetilde{U_r} \sin\left(\omega_r t + \varphi_r\right)$ yielding the sum and the difference of the two frequencies ω_c and ω_r.

$$U_f U_r = \frac{1}{2} U_f U_r \cdot \sin\left(\left(\omega_r - \omega_f\right) t + \left(\varphi_r - \varphi_f\right)\right) + \sin\left(\left(\omega_r + \omega_f\right) t + \left(\varphi_r + \varphi_f\right)\right). \quad (13)$$

With the following low-pass filter the frequency $\omega_r + \omega_f$ is cut off and the difference frequency is received. We employed a second order low-pass filter with a bandwidth of 1.6 kHz. In a locked PLL circuit ω_r and ω_f are the same ($\omega_r - \omega_f = 0$). Therefore the multiplier followed by a lowpass filter extracts the phase difference $\triangle\varphi$ out of the two signals U_f and U_r :

$$U_f U_r = \frac{1}{2} U_f U_r \cdot \sin\left(\varphi_r - \varphi_f\right) \approx \frac{1}{2} U_f U_r \cdot \triangle\varphi \qquad \text{for } \triangle\varphi \ll 1. \quad (14)$$

E.g. if there is no phase shift, the output of the multiplier is 0 V. Further, the output voltage depends linear on the phase-shift, if $\triangle\varphi$ is sufficiently small. Hence using this voltage output it is possible to follow the frequency-shift by setting the frequency generator on a new output frequency that should cancel out the frequency shift, i.e. the PLL works.

2.2.3 Proportional-Integral Controller

The proportional-integral controller processes the signal that corresponds to the frequency shift. The integral part I is realized by a capacitor as sketched in Fig.18. The proportional part P multiplies the signal, i.e. it sets the magnitude of correction.

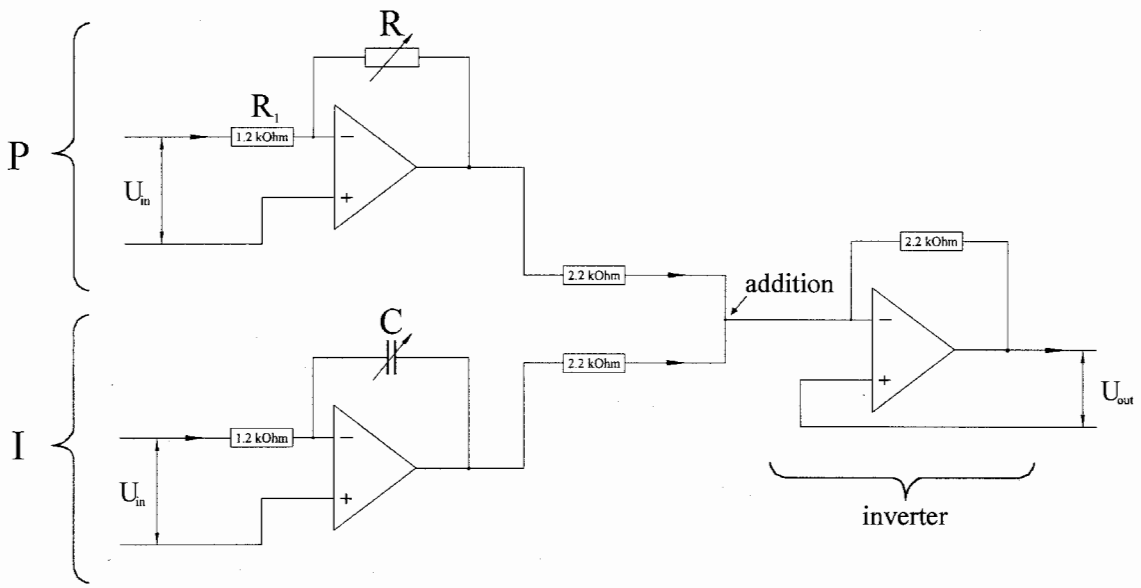

Figure 18: The diagram shows the setup of the P-I-controller. The proportional part is realized by a variable resistance and the integral part by a variable capacitor.

Mathematically the function of the P-I-controller can be expressed by

$$U_{\text{out}}(t) = P \cdot U_{\text{in}}(t) + I \cdot \int_0^t U_{\text{in}}(t)\, dt, \quad (15)$$

where U_{in}, U_{out} are the in- and output voltage, $P = R/R_1$ is the proportional factor and $I = 1/R_1C$[10] is the weight of the integrator. Differentiating Eq.15 on both sides and transforming from time to frequency space, it turns out

$$\frac{U_{\text{out}}(\omega)}{U_{\text{in}}(\omega)} = \frac{I + i\omega P}{i\omega}. \tag{16}$$

The threshold values are

$$\text{for } \omega \to \infty : \left|\frac{U_{out}(t)}{U_{in}(t)}\right| \to P \tag{17}$$

$$\text{for } \omega \to 0 : \left|\frac{U_{out}(t)}{U_{in}(t)}\right| \to \frac{I}{\omega} \tag{18}$$

The transition from the P dominated to the I dominated regime is placed at

$$f_o = \frac{I}{2\pi P} = \frac{1}{2\pi RC}, \tag{19}$$

using $f = \omega/2\pi$. The schematic plot in Fig.19 shows the characteristics of the P-I-controller.

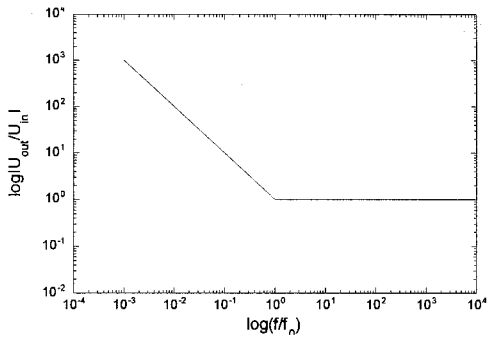

Figure 19: Schematic plot of the normalized voltage vs. normalized frequency to show the effect of the P-I-controller. For simplicity P and I are chosen to be one.

By increasing the capacity of the integrator the integrating process slows down the PLL and limits the scanning velocity. Increasing the resistance in P amplifies the $\triangle f$ signal and the PLL reacts faster, but the PLL looses stability, because interfering noise gets multiplied, too. Hence, the skill is to find parameters that the PLL works stable and fast. Typical values for topographic scanning (Fig.39) are $C = 7\,\mu\text{F}$ and $R = 30\,\text{k}\Omega$ as listed in the appendix.

2.2.4 Voltage Divider

The original setup by Nanosurf is designed for a lock range of 183.11 Hz. Fig.12 on page 15 shows that there are two frequency dependent changes of the phase, about 45 Hz apart from each other. The PLL tries to lock on the phase flip with negative slope that

corresponds to the maximum amplitude of the fork. As shown in Fig.12, the lower and upper branch of the resonance are within the lockrange. It is possible that the PLL leaves the resonance-branch with negative slope, seeks on the higher frequency end for a negative slope and cannot lock. To stabilize the PLL the lock range is reduced below the gap between the phase branches. For that reason we built in a voltage divider of factor 10 to restrict the lockrange below 20 Hz .

2.2.5 Frequency Generator

The purpose of the frequency generator is to stimulate the tuning fork. The frequency generator works digital and is included in the "Nanosurf package".

First the input voltage that corresponds to the frequency-shift $\triangle f$ gets converted by the ADC. The resolution of the ADC is 2^{15}bit and the converting factor is:

$$1\,\mathrm{V} \widehat{=} 18.311\,\mathrm{Hz}\,. \tag{20}$$

We observed with an oscillograph a strange behavior of the input signal as drawn in Fig.20. The most conspicuous characteristic of the signal is the square wave shape. The drop of the voltage is caused by the "sample and hold" mechanism of the ADC and is of no influence to our measurement. The noise of the signal could be minimized to $\pm$10mHz rms.

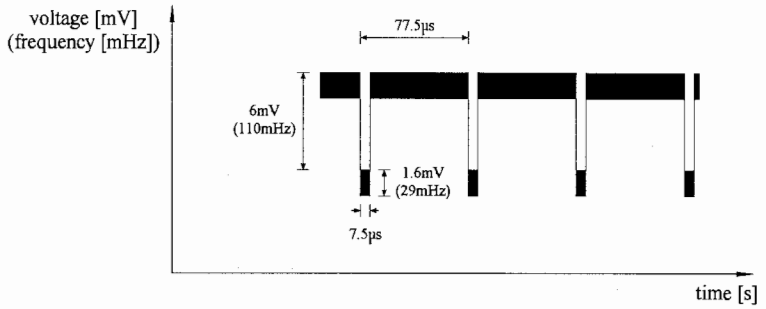

Figure 20: Drawing of the voltage signal that correspondes to the frequency-shift $\triangle f$ in the PLL. The drop of the voltage is caused by the "sample and hold" mechanism of the ADC and is of no influence to our measurement.

After passing the ADC the correction signal is added to the former centerfrequency and the new frequency leaves the digital controlled oscillator (DCO) and DAC as an ac voltage of 10VPP. The output ac voltage of the frequency generator stimulates the fork at its shifted resonance frequency. The resolution of the function generator is 5.6mHz .

2.3 z-Feedback Loop

If the PLL is locked and the center frequency of the withdrawn fork is set exactly, the voltage output of the multiplicator corresponding to the frequency-shift $\triangle f$ should vanish. While approaching the tip to the sample $\triangle f$ changes due to the force acting on the fork with the tip on it. We like to keep the tip at a fixed distance away from the sample. By keeping $\triangle f$ constant on a defined value, the distance remains constant between the tip and a point on the surface. The defined fix value of $\triangle f$ is called setpoint. While scanning the frequencyshift $\triangle f$ is kept constant on its setpoint by elongating and contracting the piezo tube. This process of keeping $\triangle f$ constant on its setpoint is implemented in a loop called z-feedback loop. The z-feedback loop is a component of the digital Nanosurf electronic and is connected to the PLL as shown in Fig.11. The sensitivity of the z-feedback is set by a P-I-controller. Usually a setpoint of 0.2 Hz is used, 20 times the noise in the signal of the PLL. Fig.21 shows the frequency-shift $\triangle f$ depending on the tip-sample distance z. The setpoint is marked by a circle. In this example the z-feedback loop keeps the tip-sample distance constant at 4 nm.

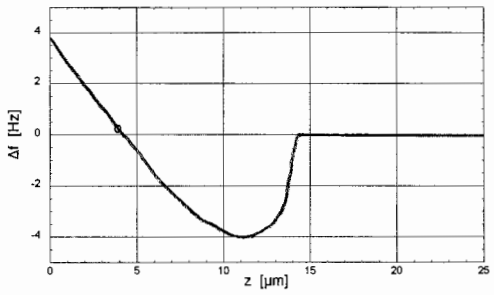

Figure 21: Plot of the frequency-shift $\triangle f$ vs. distance between tip and sample. This plot is taken out of the measurements of Fig.29 where graphite was investigated by a tungsten tip at room temperature, room pressure and no external applied voltage difference between tip and sample. The circle on the graph indicates the setpoint of 0.2 Hz and the corresponding nearest tip-sample distance of 4 nm .

Under the assumption that the character of the potential between tip and sample is everywhere the same it follows that the tip-sample distance is correlated to $\triangle f$ globally. For topography the tip is moved over the surface, keeping $\triangle f$ on its setpoint. The voltage signal that drives the piezo tube to keep $\triangle f$ on its setpoint is recorded. The voltage signal[4] corresponds to the real structure of the sample surface. Unfortunately the assumption above is in general not correct, there are impurities or localized charges that change the tip-sample potential locally. By keeping $\triangle f$ on its setpoint while scanning, the tip-sample distance can change if the potential changes and thus the achieved pictures can be falsified.

[4]The raw voltage signal has to be processed twice:

- First, subtract the voltage corresponding to the scanning movement.
- Second, we have to take into account that during the scanning process the tip-sample distance changes due to the bending away of the tube. Hence we have to subtract the voltage that compensates the bending.

3 Operation of the SFM

The operation of the SFM is treated in detail in the appendix "*Bedienungsanleitung für selbstgebautes SFM*". In the following sections only the basic principles of the operation of the SFM are discussed.

3.1 The Approach

The goal is to place the tip over the sample surface and to lock the z-feedback loop on its setpoint.

The approach consists of two parts, first the coarse and second the fine approach. The coarse approach is done with micrometer screws as introduced in section 1.4.3 and the fine approach is done by elongating and contracting the piezo tube.

First we ensure that the PLL is locked and the tip is withdrawn by contraction of the piezo tube. Then we approach the tip as close as possible to the sample by using the micrometer screws. This procedure is observed by microscope.

We define a setpoint (section 2.3) and release the tip. The piezo elongates until the frequencyshift $\triangle f$ reaches its setpoint. If the surface is too far away and cannot be reached by maximal elongation of the tube, the tip has to be withdrawn again, followed by screwing the mounting further down. This process is repeated until the sample is within the range of the piezo tube and the z-feedback is able to lock.

Because of the piezo creep (section 1.4.2) we have to wait for 30 min before we start with any measurement.

3.2 Force-Distance-Measurements

As starting point the PLL and the z-feedback have to be enabled. Then we fix the position of the tip by switching the feedback loop off, but keeping the voltage input to the piezo tube constant. By applying an additional voltage on the piezo tube the tip-sample distance can be changed. While changing the tip-sample distance the frequency-shift $\triangle f$ of the PLL changes, if a tip-sample interaction is present. The frequency shift is correlated to the potential respectively to the force interacting between tip and surface (Sec.2, part III). For this reason the recording of changes of $\triangle f$ vs. distance are called "force-distance-measurements" and the results are called "force-distance-curves".

3.3 Topographic Scanning in Dynamic Mode

First the PLL and z-feedback have to be enabled. Scanning the surface while the z-feedback loop is locked gives us information about the structure of the surface. Bear in mind that the achieved picture of the surface is not the real topographic structure as shown in section 2.3.

Part II
Tip Preparation

1 Etching Setup

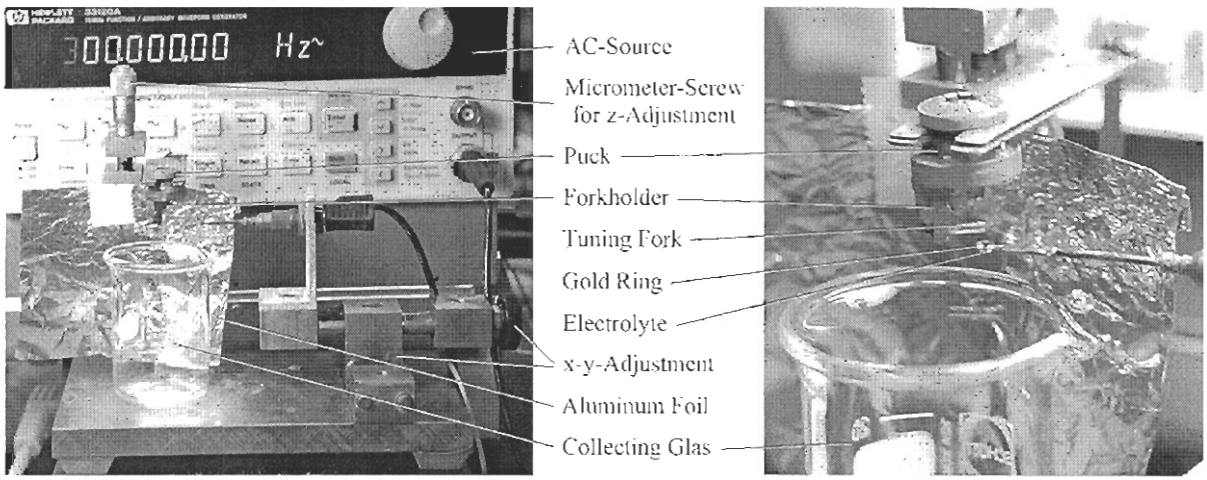

Figure 22: The left picture gives an overview of the etching setup and the picture on the right side shows the tuning fork placed over the gold ring.

In STM it is sufficient to have rather "blunt" tips to achieve resolution of the order of Å. Because the tunneling current falls off exponentially in the nonconducting region between tip and sample, the current takes always the shortest way through the barrier, i.e. the current chooses always the foremost atom and leaves the rest of the tip surface almost untouched. A disadvantage of the STM is that tip and sample must be conducting. In SFM the imaging signal is the force F_{ts} between a tip and a surface. F_{ts} can be of long range and *all* atoms of the front of the tip interact with the sample in contrast to STM. Therefore SFM tips need to be extremely sharp for producing pictures of high resolution. Obviously the preparation of tips is crucial for the operation of an SFM.

A fast, cheap and effective way to fabricate sharp and reliable tips is electrochemical etching[6] of metal wires. The etching setup is sketched in Fig.22. The picture on the right side shows a fork fixed at the puck and under the fork a gold ring is mounted holding a drop of electrolyte. The wire glued at the end of the tuning fork (Fig.14) is placed over the ring by using the x-y-adjustment, then the wire gets immersed in the electrolyte by turning the micrometer screw on the top of the setup. Then the tip is etched by applying a voltage between the wire in the electrolyte and the ring electrode.

I focused on etching Pt90/Ir10 (90% Platinum and 10% Iridium) and W-tips. Tungsten is a very hard metal of a tensile strength of 1920MPa compared to the softer Pt90/Ir10 of tensile strength of $380 - 620$MPa. The hardness of tungsten is favorable because the tip does not deform as fast as the Pt90/Ir10 tip, but the drawback is that Tungsten oxidizes in air in contrast to the inert Pt-Ir.

The stiffness of the wires made of these materials is directly correlated to their hardness and the diameter of the wires. We desire to have wires as stiff as possible such that they

do not vibrate while scanning. But on the other side we desire to affix wires on the fork that are as light as possible, because additional weight on one fork arm influences the properties of the resonances of the fork negatively. The decrease in weight can be achieved by reducing the diameter of the wire, but this causes a decrease in stiffness. Calculating the resonance properties of wires of the length of 200 μm - 500 μm with the tools in Ref.[2] and demanding a lowest resonance frequency higher than the lowest resonance of the system (i.e. the piezo tube) it turns out that a diameter of 13 μm for the tungsten wire and 25 μm for the Pt90/Ir10 wire is sufficient.

Some more interesting data[27]on the used materials are

	W	Pt90/Ir10
Photoelectric Work Function	4.55 eV	
Density at 20 °C	19.3 g cm^{-3}	21.56 g cm^{-3}
Electrical Resistivity	5.4$\mu\Omega$ cm	25$\mu\Omega$ cm
Tensile Strength	380 – 620M Pa	1920M Pa

2 Etching of Tungsten Wires

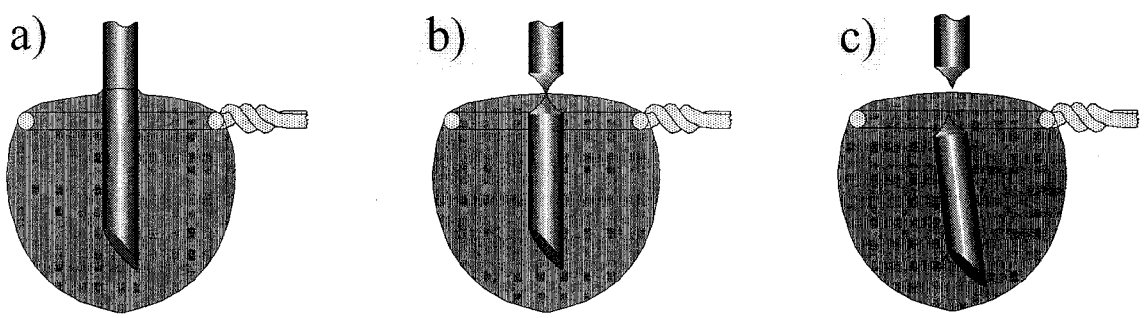

Figure 23: Schematic etching process of a tungsten wire. a) the wire is immersed in KOH, then ac voltage is applied and the etching starts mainly at the contact surface between electrolyte and air. If the insection is tight enough the lower part of the wire drops off and a new tip is manufactured after switching off the voltage and pulling back the wire.

First the wire is cleaned in HCl. As schematically drawn in Fig.23a the wire is approached from above and partially immersed in 1-molar KOH hanging on a ring. The ring made out of gold is more noble than tungsten therefore the electrolyte does not corrode the gold. The drop of electrolyte is hanging on the ring hold by adhesive surface forces. By applying an sinusoidal ac voltage of 3 V with a frequency of 300 Hz between wire and gold ring the tungsten wire gets etched. Because the wire is immersed in the middle of a ring shaped electrode the wire gets etched symmetrical under rotation. The etching process takes place mainly at the contact surface between air and electrolyte. The etching in this restricted region as sketched in Fig.23b leads to an insection of the wire until the lower part of the wire drops off. This falling off as sketched in Fig.23c is observed by microscope and used as a criterion for stopping the etching process, i.e. turning off the voltage. After pulling back the tip we clean it with HCl followed by distilled water. If

the electrolyte splashes on the fork while etching, a piece of scotch tape can be fixed as a shield on the lower arm of the fork.

The typical shape of a Tungsten tip is shown in Fig.26 on the upper right and the lower picture shot by TEM. The picture shot by SEM on the upper left side in Fig.26 shows the typical concave shape on macroscopic scale. The tip shapes and sharpness are reproducible. The lower picture in Fig.26 shows a thin tungsten-oxide film on the tip covered by a carbon film. The carbon, an ingredient of vacuum grease in the vacuum chamber, grew as a film on the tip under influence of the electron beam of the SEM or TEM, respectively. Fig.24 confirms the statement above: the SEM picture on the left shows a pure tip, after waiting 20 min a carbon film of 100 nm thickness grew on the illuminated area as showed in the picture on the right. It follows that an etched tip is covered only by an oxide film as long we do not put it in a SEM or TEM. Hardly ever

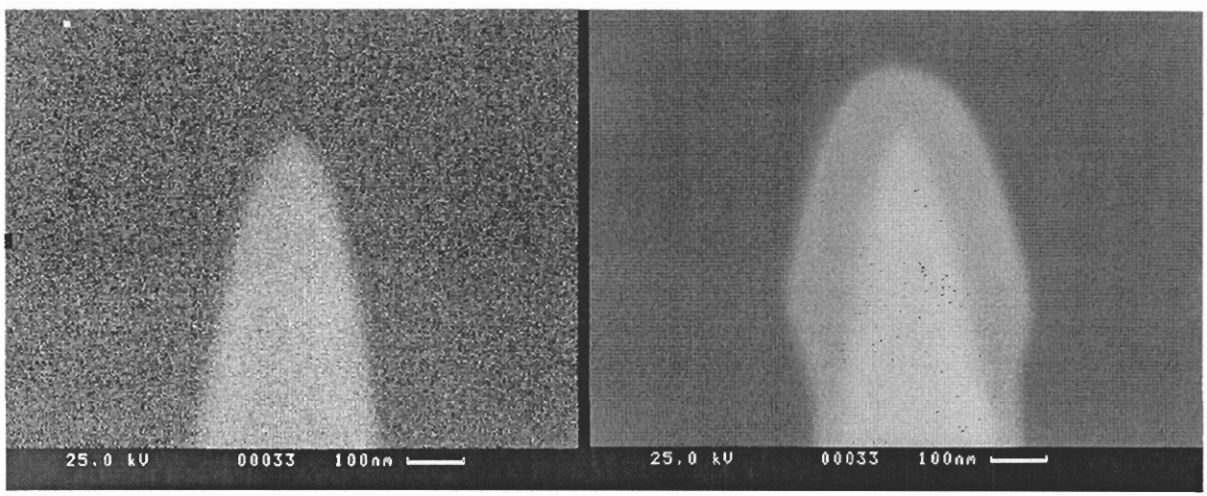

Figure 24: Pictures of a tungsten tip shot by SEM. The picture on the left shows a brand new tip. The picture on the right shows the tip after 20 min exposed to the SEM beam. In the illuminated area a 100 nm thick carbon film grew on the tip.

a miraculous rolling up of the tip occurs as displayed in the picture on the front page, indicating a nonuniform tension in the wire, probably due the fabrication by drawing. To sum up, with this simple method tips with diameters smaller than 50 nm and a very regular shape can be produced easily.

3 Etching of Platinum/Iridium Tips

Etching Pt-Ir tips requires a more sophisticated technique than the processing of tungsten wires described in the preceding section. The etching of Pt-Ir wires is split in two parts: first, the pre-etching and second, the final etching.

The first part of this two step process is exactly the same procedure as mentioned above for tungsten except that we used instead of KOH the solution[5] $KCL/H_2O/HCl$. Contrary to the etching of W-tips we have no longer the useful effect of the etching in a restricted area at the surface. The etching process takes place everywhere on the immersed

[5]dissolve 2g KCL in 8.37ml H_2O and add about two drops of HCL(15%)

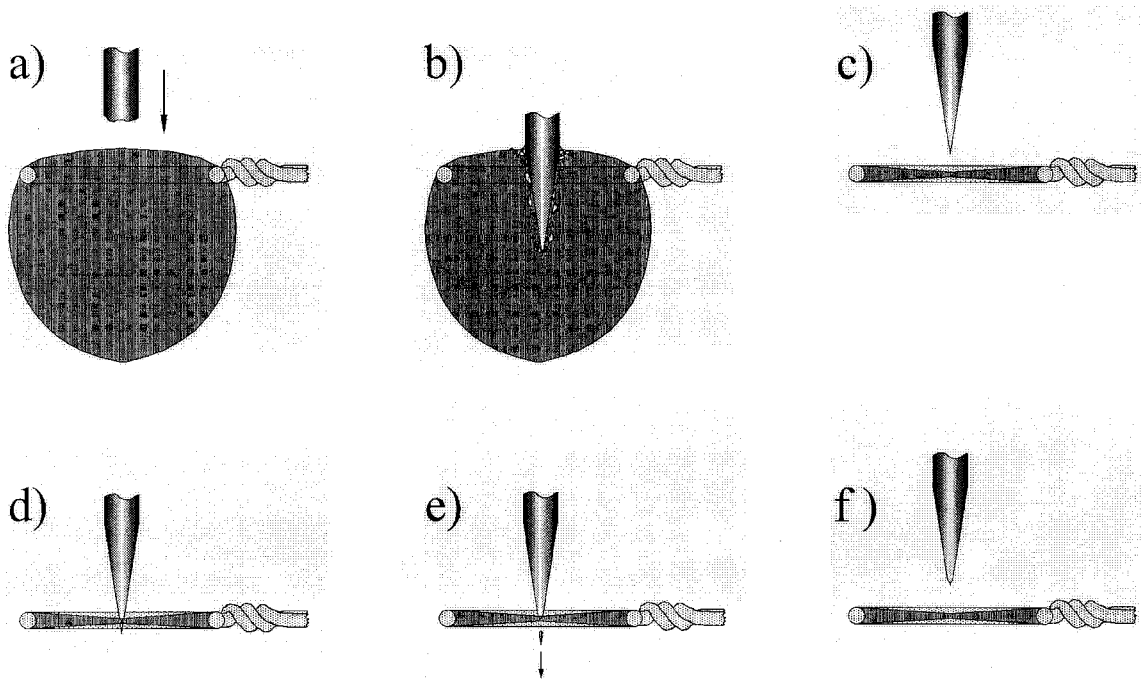

Figure 25: Schematic etching process of platinum-iridium wires.

wire (Fig.25b) and we have not the falling off of the lower end of the wire if the insection is thin enough as seen on tungsten. Unfortunately tips with a minimal diameter of 100 nm were fabricated by applying the first step, obviously much too blunt for our purpose.

For that reason we developed a second step, Fig.25c-25f. The drop of the electolyte in the gold ring gets absorbed by a piece of a kleenex until there is only a thin membrane left. The tip is immersed in the membrane such that only the foremost part of the tip reaches out of the lower side. Then by turning on the voltage, the tip is etched locally and the foremost part of the tip drops off if the etched insection is thin enough. Using this technique tips usually sharper than 50 nm in diameter were achieved. Fig.27 shows us that the shape of the tips are not as regular as observed for the tungsten tips and we observed that the tips formed sometimes double tips. An advantage of the Pt-Ir material is that it is possible to manufacture tips well below 10 nm as shown in the lower picture in Fig.27 and that no oxide layer covers the tip. On the lower pictures in Fig.27 a carbon film covering the tip can be recognized again, but as discussed in the preceding section the origin of this film is the observation with the SEM and TEM.

4 Conclusion

In conclusion the quality of our tips is very satisfying compared with results of others, e.g. in Ref.[11], where the chemical process of the etching of Pt-Ir tips is treated in detail, but tips of only 150 nm in diameter were reached.

For topography scanning we used the sharp Pt-It tips, although they are soft and difficult to fabricate. For distance dependent force investigation we prefer tungsten tips, because sometimes tip-crashes occur during the measurements and due to the hardness of tungsten the tips remain undamaged for a longer period of time than the Pt-Ir tips.

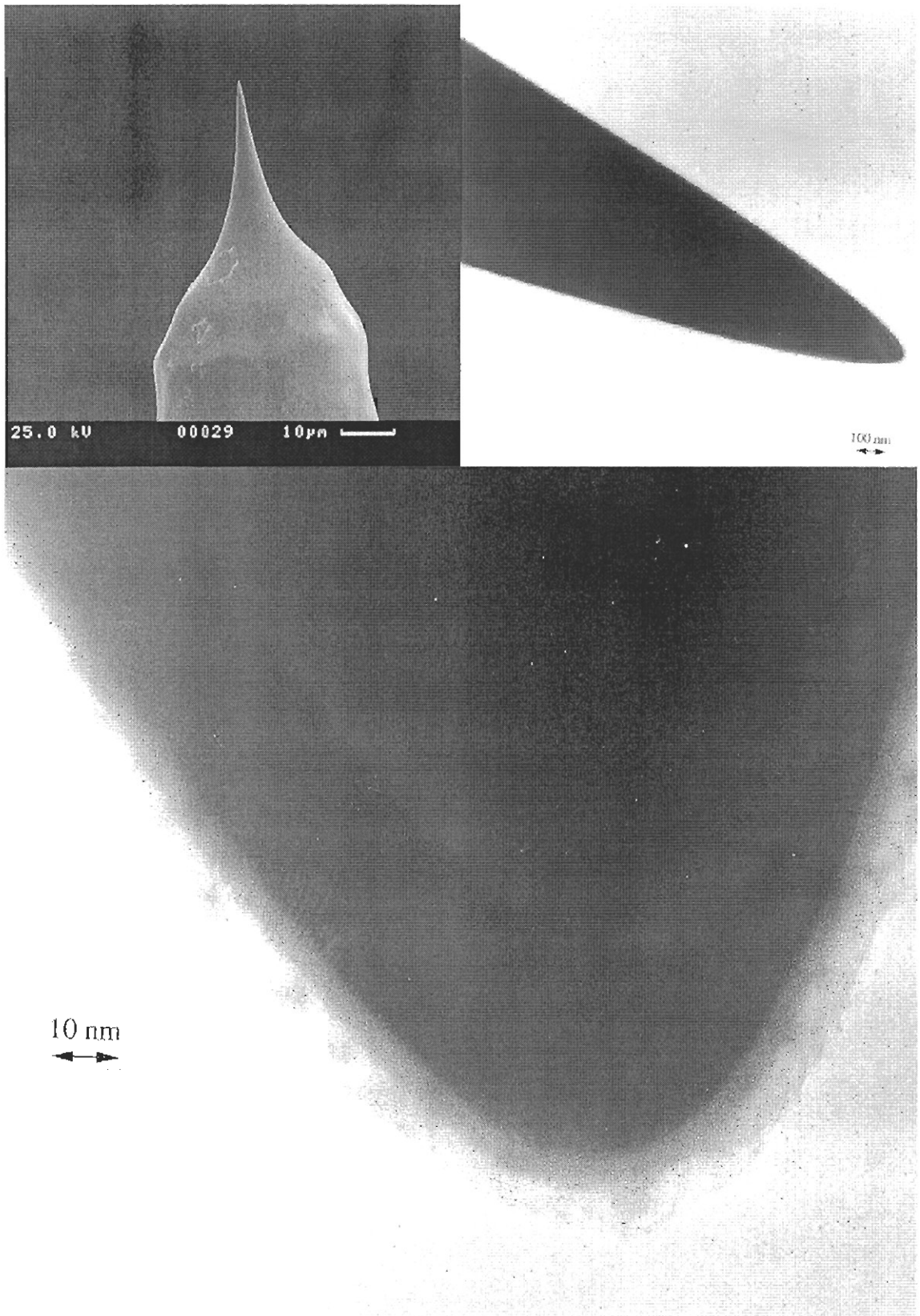

Figure 26: SEM and TEM pictures of a tungsten tip. On the lower picture it can be recognized that the tip is covered by an oxide film followed by a carbon film.

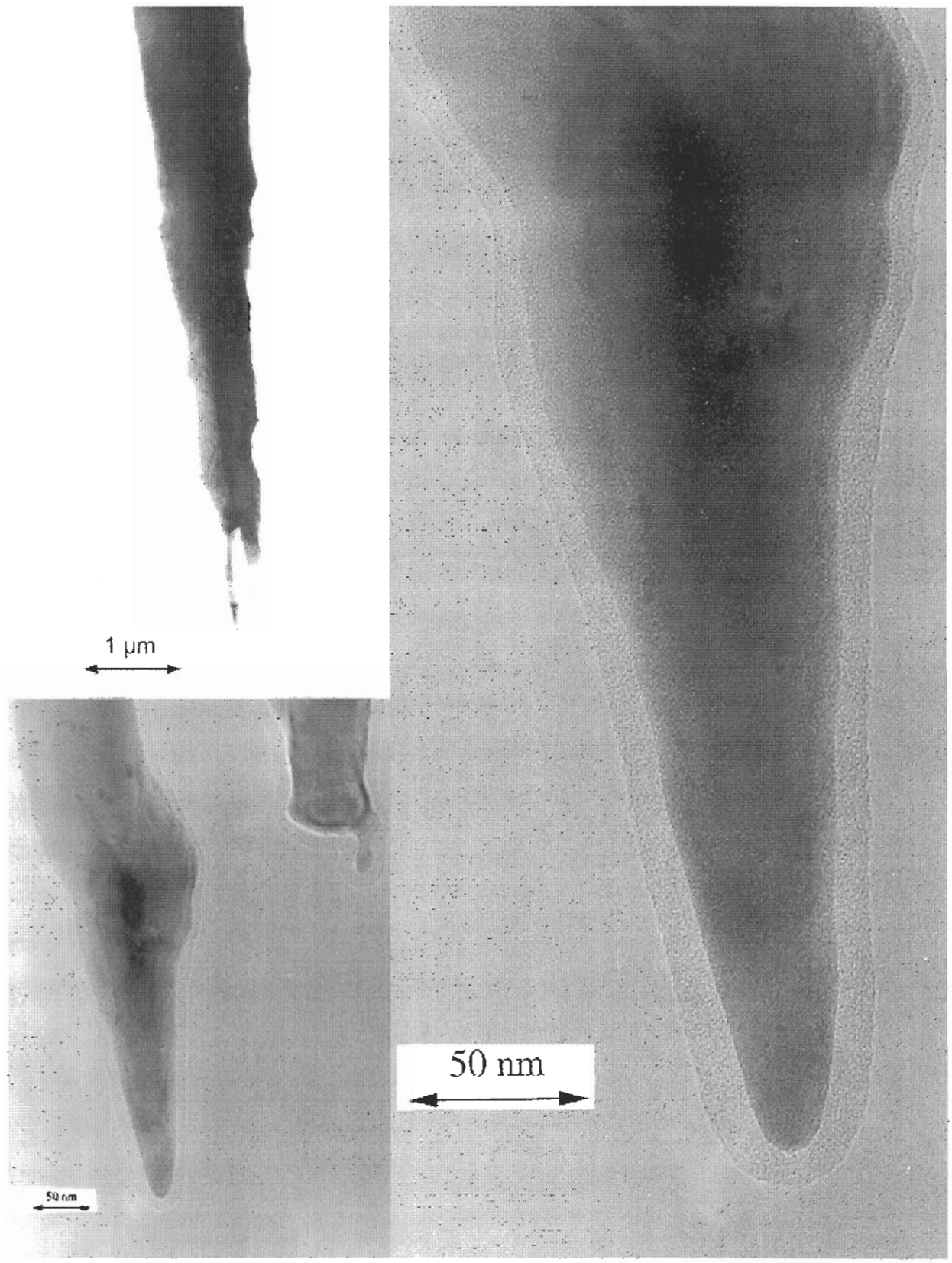

Figure 27: SEM and TEM pictures of a Platinum-Iridium tip. The tip is covered by a carbon film.

Part III
Force-Distance-Measurements

First tip-sample distance dependent measurements of the frequency shift $\triangle f$ of the tuning fork are presented. Then the correlation between $\triangle f$ and the interaction potential is deduced, followed by a review on several tip-sample potentials. Finally the measurements are discussed based on the results of the preceding sections.

1 Measurements

We measured the frequency shift $\triangle f$ as a function of the tip-sample distance at one single point on the sample. Each measurement was recorded under a pressure of 10^{-4} mbar and at room temperature, without heating the sample. The amplitude of the tuning fork oscillation was about 10 nm. The zero point of the z-axis was chosen to lie on the surface of the sample. The choice of the zero point is justified in section 4.1 and 4.2.

1.1 Gold Surface Investigated with Platinum/Iridium Tip

Fig.28 shows the result of the investigation of a Gold-surface with a Platinum/Iridium tip. The frequency shift $\triangle f$ is plotted versus the tip-sample distance z. The sample is a Gold Au(111) film on a mica substrate, 200 nm thick from the supplier Nanosurf [15]. The frequency shift was recorded while driving the tip away from the sample surface.

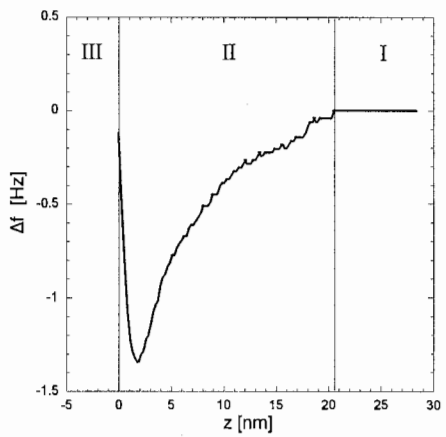

Figure 28: Measurement of the frequency-shift $\triangle f$ versus distance. The investigated material is a Gold film and the tip consists of Pt-Ir.

Fig.28 is divided in three regions. In region I the fork does not feel any force acting on it and thus $\triangle f = 0$. In region II the frequency shift is nonzero. At about 20 nm the frequency shift starts to decrease until a minimum is reached at 2 nm. After passing the minimum value $\triangle f\,(2\,\text{nm}) = -1.34\,\text{Hz}$ the frequency shift increases with a steep slope towards the zero point of the coordinate system. Region III was not accessible for our measurements without tip crashes, indicating that region III coincides with the sample surface.

1.2 Graphite Surface Investigated with Tungsten Tip

Fig.29 shows the result of the investigation of a graphite (HPOG) surface with a tungsten tip, the frequency shift $\triangle f$ is plotted versus the tip-sample distance z. The HPOG surface was prepared by pulling away the top layers after fixing them on a scotch tape. The frequency shift was recorded while driving the tip towards the sample surface. Additionally, potential differences of different values were applied between tip and sample. The voltage was applied to the sample and the tip was virtually grounded by connecting it to an electrode of the fork arm. The applied dc voltages were $-7\,\mathrm{V}$, $-5\,\mathrm{V}$, $-3\,\mathrm{V}$, $0\,\mathrm{V}$, $3\,\mathrm{V}$ and $5\,\mathrm{V}$.

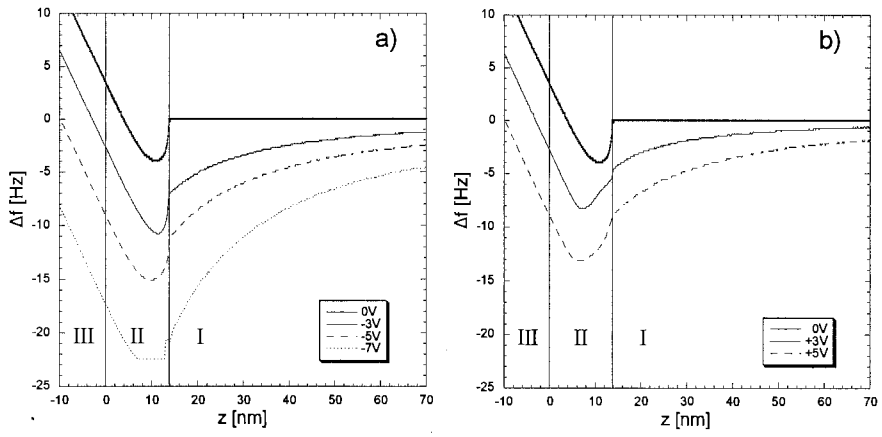

Figure 29: Measurements of the frequency shift $\triangle f$ versus tip-sample distance. The HPOG sample was investigated with a tungsten tip. On the left plot negative voltage differences between tip and sample were applied, on the right plot positive voltages were applied.

Fig.29 is divided into three regions. At an applied voltage of $0\,\mathrm{V}$ no frequency shift occurs in region I. At the transition from region I to region II at $14\,\mathrm{nm}$ the frequency shift drops downwards and reaches the minimum value of $-4\,\mathrm{Hz}$ at $11\,\mathrm{nm}$. After passing the minimum the curve increases by approaching the tip closer to the surface and after about $6\,\mathrm{nm}$ the increase of $\triangle f$ is linear. In region III the linear increase of $\triangle f$ continues.

For all applied nonzero voltages between tip and sample the values $\triangle f$ are shifted downwards, without regard to the sign of the voltage. In region I the applied voltage leads to a smooth decrease of the frequency shift, indicating that the arising force on the tip is of long range. At the transition from region I to region II the abrupt decrease of $\triangle f$ arises again as observed in the zero voltage measurement. (The little difference in the structure of the negative slope of the curve in region II, Fig.29b is due to a major tip crash after having accomplished the measurements at negative voltages.) After passing the minimum the slope of the increase of $\triangle f$ is linear and parallel to the other measurements. In region III the curves are all parallel with the same linear behavior.

The $-7\,\mathrm{V}$-curve in Fig.29a is cut-off at $-22.5\,\mathrm{Hz}$ due to the limitation of the measuring range (section 2.2.4, Part I). To show the dependence of the frequency shift on the applied voltage we plotted in Fig.30 $\triangle f$ versus voltage at four fixed tip-sample distances. The chosen distances are indicated in Fig.30a (same plot as Fig.29a) as vertical lines at 5, 10, 30 and $40\,\mathrm{nm}$. On the right plot of Fig.30 the connected points show the shape of a parabola with the aperture towards negative $\triangle f$-values. The parabola recorded far away

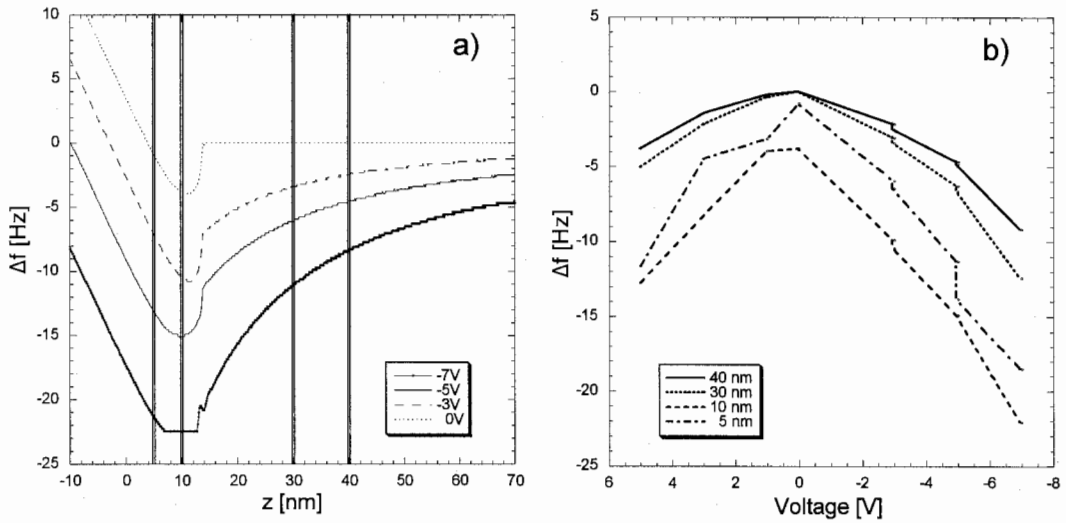

Figure 30: a) $\triangle f$ versus distance for different voltages applied between W-tip and HPOG-surface. b) $\triangle f$ versus applied voltage at fixed z-values. The fixed z-values are marked by the vertical lines in the plot on the left.

from the surface show bigger apex radii than the curves closer to the sample surface. Due to tip deformations due tip crashes between the measurements (section1, Part V) the data close to the surface are not as reliable as the data taken at larger distances, because the specific shape of the tip has not a such big influence on the interactions at larger distances. At a closer look the parabolas are shifted about $0.2 - 0.4\,\mathrm{V}$ towards positive voltages.

Fig.31 shows the data from the measurements above plotted in a three dimensional frame. The measured data were interpolated to achieve a smooth plane between the curves.

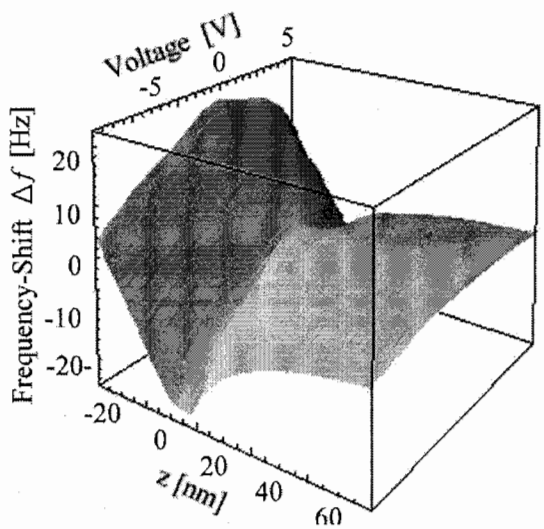

Figure 31: The three-dimensional plot shows the measurement of the frequency-shift $\triangle f$ depending on distance z and applied voltage V.

2 Correlation between Frequency-Shift $\triangle f$ and Interaction Potential

In part 1 we noticed that the frequency of the tuning fork is shifted in the presence of a tip-sample interaction potential. It is of fundamental interest to find the correlation between the frequency shift and the interaction potential. Here we present a computation based on perturbation theory inspired by the work of F.J.Giessibl, Ref.[5].

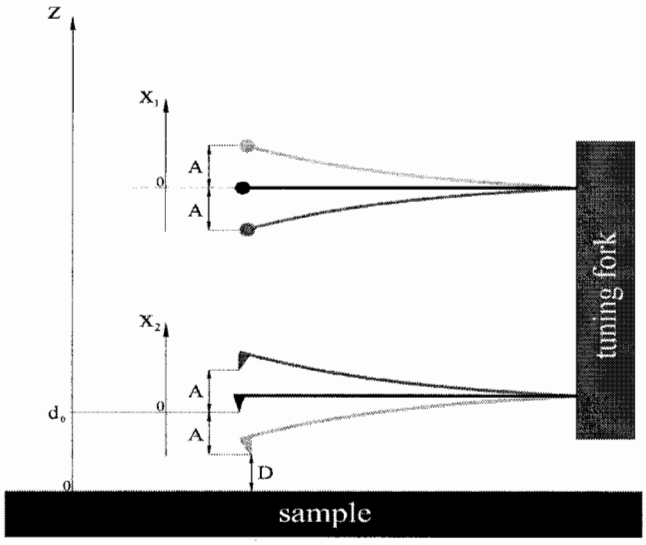

Figure 32: Schematic drawing of the tuning fork as two coupled pendula vibrating over a surface.

The notations used in this section are defined in Fig.32. A is the oscillation amplitude and the quantity d_0 is defined as the distance between tip and sample if the arm of the tuning fork is undeflected. The tip-sample distance at the point of closest approach is denoted as D. Remembering the model of a tuning fork in section 2.2.1, part I we define the deflection of the upper arm as x_1 and the deflection of the lower arm as x_2. The actual tip-sample distance is defined as $z \equiv d_0 + x_2$, where the z-axis is perpendicular to the sample surface and its zero point lies on the sample surface.

2.1 Equation of Motion

In section 2.2.1, part I, we introduced a model of two coupled pendula to describe the tuning fork by the equations of motion

$$\begin{aligned} m\ddot{x}_1 + k_a x_1 + \tfrac{1}{2}k_c (x_1 - x_2) &= 0 \\ m\ddot{x}_2 + k_a x_2 + \tfrac{1}{2}k_c (x_2 - x_1) &= 0, \end{aligned} \tag{21}$$

where m is the effective mass and k_a the spring constant of a single tuning fork arm, k_c is the coupling between the two arms and x_1, x_2 are the deflections of the upper and the lower arm, respectively.

In reality the two masses of the fork arms are in most cases not of the same weight due to the gauging of the fork on its resonance of 2^{15} Hz by cutting off weight on its arms.

By fixing a wire on one arm the masses become certainly different and therefore we have to modify the equation of motion above by introducing two different masses m_1 and m_2:

$$\begin{aligned} m_1\ddot{x}_1 + k_a x_1 + \tfrac{1}{2}k_c\,(x_1 - x_2) &= 0 \\ m_2\ddot{x}_2 + k_a x_2 + \tfrac{1}{2}k_c\,(x_2 - x_1) &= 0. \end{aligned} \tag{22}$$

We obtain the Eigenfrequencies of the equations of motion above (see Appendix):

$$\Omega_{1,2}^2 = \left(k_a + \frac{k_c}{2}\right)\frac{m_1 + m_2}{2m_1m_2} \pm \sqrt{\left(k_a + \frac{k_c}{2}\right)^2\left(\frac{m_1 - m_2}{2m_1m_2}\right)^2 + \frac{k_c}{4m_1m_2}} \tag{23}$$

and the Eigenvalues

$$q_1 = e_{11}\cdot y_1 + e_{21}\cdot y_2 \tag{24}$$

$$q_2 = e_{12}\cdot y_1 + e_{22}\cdot y_2, \tag{25}$$

where

$$e_{11} = e_{22} = \sqrt{\frac{1}{1+h^2}} \qquad \text{and} \qquad e_{12} = -e_{21} = \sqrt{\frac{h^2}{1+h^2}} \tag{26}$$

using the definitions

$$y_i \equiv \sqrt{m_i}x_i, \quad h \equiv \kappa + \sqrt{1+\kappa^2} \quad \text{and} \quad \kappa \equiv \frac{k_a + \frac{k_c}{2}}{\frac{k_c}{2}}\frac{m_1 - m_2}{2\sqrt{m_1m_2}}. \tag{27}$$

In the limit $m_2 \longrightarrow m_1 \equiv m$ the expressions above reduce to the well known result

$$\text{asymmetric mode} \;:\quad q_1 = \frac{1}{\sqrt{2}}\,(y_1 - y_2) \tag{28}$$

$$\text{symmetric mode} \;:\quad q_2 = \frac{1}{\sqrt{2}}\,(y_1 + y_2) \tag{29}$$

with the corresponding Eigenfrequencies

$$\Omega_{1,2}^2 = \frac{1}{m}\left(k_a + \frac{k_c}{2}\right) \pm \frac{k_c}{2m} \tag{30}$$

2.2 Perturbation Theory

To compute the correlation between the frequency shift $\triangle f$ and the interacting potential we apply perturbation theory. Starting with the unperturbed Hamiltonian

$$H_0\,(p_1, p_2, q_1, q_2) = \frac{1}{2}p_1^2 + \frac{1}{2}p_2^2 + \frac{1}{2}\Omega_1 q_1^2 + \frac{1}{2}\Omega_2 q_2^2 \tag{31}$$

describing the system (22) and applying the perturbation

$$H_1 = V_{ts}\,(d_0 + x_2)\,, \tag{32}$$

we obtain

$$\frac{\triangle f_i}{f_i} = \frac{e_{i2}}{2E_i\sqrt{m_2}} \langle F_{\text{ts}} (d_0 + x_2) q_i \rangle \tag{33}$$

where $\triangle f_i$ is the frequency shift of the tuning fork, f_i is the center frequency, E_i is the energy of the mode i and $F_{\text{ts}} \equiv -\nabla V_{\text{ts}}$. The derivation is shown in the Appendix "Computations". Eq.33 is a generally valid result.

For practical use we like to simplify Eq.33. Assuming that $m_1 = m$ and $m_2 = m + \triangle m$ with $\triangle m/m \ll 1$ and using Eq.81 (Appendix) we obtain a criterion

$$\frac{\triangle m}{m} \ll \frac{k_{\text{c}}}{k_{\text{a}}} \tag{34}$$

for which we can reduce the problem with two different masses to the problem with equal masses. The statement of the criterion above is that we can simplify Eq.33 only if the relative mass asymmetry of the two tuning fork arms is much smaller than the relative coupling strength of the two arms. From the estimations in section 2.2.1, part I, we obtain $k_{\text{a}} = 8850\,\text{N/m} \pm 1380\,\text{N/m}$, $k_{\text{c}} = 2510\,\text{N/m} \pm 2460\,\text{N/m}$ and $m = m_{\text{eff}} = 0.268\,\text{mg} \pm 0.048\,\text{mg}$. Using the data from the table on page 27 we are able to estimate the additional mass due to the tip on the lower fork arm. As mentioned in part II we work with tips made of W- or Pt/Ir-wires, their density is $\rho_{\text{W}} \approx \rho_{\text{Pt/Ir}} \approx 20\,\text{g cm}^{-3}$. Assuming that the length of the wire on the fork arm is about $500\,\mu\text{m}$ and knowing that the diameter of the W-wire is $13\,\mu\text{m}$ and the diameter of the Pt/Ir-wire is $25\,\mu\text{m}$ we obtain

$$\frac{\triangle m_{\text{W}}/m}{k_{\text{c}}/k_{\text{a}}} = 1.8 \cdot 10^{-3} \ll 1 \tag{35}$$

$$\frac{\triangle m_{\text{Pt/Ir}}/m}{k_{\text{c}}/k_{\text{a}}} = 6.3 \cdot 10^{-3} \ll 1. \tag{36}$$

Because the deviations in the estimated values above are enormous we calculate the expression above again for the worst case, i.e. for a Pt/Ir-wire, minimal m, maximal k_{a} and minimal k_{c} and we obtain for the ratio between the relative mass asymmetry and the relative coupling strength a value of $0.456 < 1$. Thus the condition is fulfilled and we can now simplify expression (33).

Since the tuning fork of the SFM is stimulated at its asymmetric resonance (Fig.17 and 32) we focus on the influence of the interaction force to the frequency shift of this mode. Thus we derive from Eq.33 an expression that correlates the relative frequency shift of the first mode with the mean value of the interaction force

$$\left.\frac{\triangle f}{f_0}\right|_{\text{asymm}} = -\frac{1}{(k_{\text{a}} + k_{\text{c}})\, A^2} \langle F (d_0 + x_2)\, x_2 \rangle, \tag{37}$$

where we replaced $E_1 = \frac{1}{2} k_1 A^2$, using the maximal potential energy of a harmonic oscillator.

2.2.1 Application to Inverse Power Law potentials

In many cases, the potential between tip and sample can be well described by an inverse power law

$$V_{\mathrm{ts}}(z) = -\frac{C_{\mathrm{n}}}{z^n} \tag{38}$$

where $z = x_2 + d_0$ is the tip-sample distance and C_n is a characteristic constant depending on the properties of the material of the tip and sample. The interaction force between tip and sample is obtained by $F_{\mathrm{ts}} = -\nabla_z V_{\mathrm{ts}}$. Inserting F_{ts} obtained from Eq.38 in Eq.37, taking the average for a full oscillation period and applying $x_2(t) = A\cos(2\pi f_0 t)$ we obtain

$$\left.\frac{\triangle f}{f_0}\right|_{\mathrm{asymm}} = \frac{1}{2\pi}\frac{nC_{\mathrm{n}}}{(k_{\mathrm{a}}+k_{\mathrm{c}})AD^{n+1}}\int_0^{2\pi}\frac{\cos(x)}{\left(1+\frac{A}{D}(\cos(x)+1)\right)^{n+1}}dx, \tag{39}$$

where we substituted $d_0 = D + A$ as depicted in Fig.17 with the closest distance D between tip and sample. Eq.39 can be simplified for two limiting cases:

- **Small amplitudes** $A \ll D$

$$\underline{\underline{\left.\frac{\triangle f}{f_0}\right|_{\mathrm{asymm}} \cong -\frac{n(n+1)}{2(k_{\mathrm{a}}+k_{\mathrm{c}})}\frac{C_{\mathrm{n}}}{D^{n+1}} = \frac{1}{2(k_{\mathrm{a}}+k_{\mathrm{c}})}\left.\frac{\partial^2 V_{\mathrm{ts}}(z)}{\partial z^2}\right|_{z=D}}}, \tag{40}$$

  which corresponds to the result of the force gradient method treated by H. Hölscher in Ref.[3].

- **Large amplitudes** $A \gg D$

$$\underline{\underline{\left.\frac{\triangle f}{f_0}\right|_{\mathrm{asymm}} \cong -\frac{1}{\sqrt{2}\pi}\frac{1}{(k_{\mathrm{a}}+k_{\mathrm{c}})A^{3/2}}\frac{nC_{\mathrm{n}}}{D^{n+1/2}}I_1(n+1)}}, \tag{41}$$

  with

$$I_1(n+1) \equiv \int_{-\infty}^{\infty}\frac{1}{(1+y^2)^{n+1}}dy. \tag{42}$$

  Using the fact that $\frac{\sqrt{2}}{\pi}I_1(n+1) \sim 1$ Eq.41 can be rewritten as

$$\left.\frac{\triangle f}{f_0}\right|_{\mathrm{asymm}} \cong -\frac{n(n+1)}{2(k_{\mathrm{a}}+k_{\mathrm{c}})}\frac{C_{\mathrm{n}}}{D^{n+1}}\cdot\frac{1}{n(n+1)}\left(\frac{D}{A}\right)^{3/2} \tag{43}$$

$$= \frac{1}{2(k_{\mathrm{a}}+k_{\mathrm{c}})}\left.\frac{\partial^2 V_{\mathrm{ts}}(z)}{\partial z^2}\right|_{z=D}\cdot\frac{\sqrt{2}}{n(n+1)\pi}\left(\frac{D}{A}\right)^{3/2}. \tag{44}$$

  The first term in the relative frequency shift in Eq.43 is equal to the solution of $\triangle f/f_0$ in the $A \ll D$ limit. The second term reduces the signal by a factor proportional to $\frac{1}{n(n+1)}(D/A)^{3/2}$.

3 Interaction Potentials

3.1 Particle-Particle-Interactions

Many well known particle-particle-interaction potentials are of the form of inverse power laws:

$$w(r) = -\frac{C_n}{r^n}, \tag{45}$$

where r is the particle-particle separation and C_n is a constant. The following particle-particle-interactions are examples[23] for potentials of the structure of Eq.45

$$\begin{array}{ll} n = 1: & \text{ion-ion interaction (Coulomb's law)} \\ n = 2: & \text{dipole-ion interaction} \\ n = 3: & \text{dipole-dipole interaction} \\ n = 4: & \text{induced dipole-ion interaction} \\ n = 5: & \text{induced dipole-dipole interaction} \\ n = 6: & \text{induced dipole-induced dipole interaction (van der Waals, Casimir).} \end{array} \tag{46}$$

A further example is the Lennard-Jones potential[21]

$$w(r) = -\frac{C_6}{r^6} + \frac{C_{12}}{r^{12}}, \tag{47}$$

where the attractive term is the van der Waals attraction due to fluctuating dipole interaction and the repulsive term is due the repulsion of the ion cores of the atoms.

Tip and sample are macroscopic bodies. Only under very restrictive assumptions the particle-particle interactions can be applied to describe the tip-sample interactions. We have to take into account to the tip-sample interactions the influence of the geometry of the arrangement of the molecules. Therefore a more refined treatment is necessary.

3.2 Tip-Surface Interactions

The goal of this section is to calculate the tip-sample interactions. First a model for interactions obeying inverse power laws under the assumption of additivity is introduced. Second a model of electrostatic forces is shown based on the image method of equipotentials. Third the capillary force due to a liquid bridge between tip and sample is introduced.

3.2.1 Model of Additive Inverse Power Law Interactions

Let us assume that the pair potential between two atoms or small molecules is purely attractive and of the form of Eq.45. Then, with the further assumption of additivity, the net interaction energy of a molecule and the planar surface of a solid made up of identical molecules will be the sum of its interactions with all the molecules in the body. According to Israelachvili[23] we can now calculate the interaction energy of a flat surface and differently shaped tips. We introduce two different models for a tip, a sphere and a rotation paraboloid.

The net interaction energy of sphere of radius R at a fixed distance d away from the sample surface is

$$V(d) = -\frac{2A_H}{(n-2)(n-3)} \int_{z=0}^{z=2R} \frac{(2R-z)\, z dz}{(d+z)^{n-3}} \qquad \text{for } n > 3. \tag{48}$$

The z-axis is perpendicular to the sample surface and $z = 0$ is chosen to be on the foremost point of the sphere at a distance d to the sample surface. $A_H \equiv \pi^2 C_n \rho_s \rho_t$ is the Hamaker constant, where ρ_s is the number density of molecules in the sample and ρ_t is the number density of molecules in the tip.

Fig.26 suggests to approximate the shape of the tip by a rotation paraboloid. For a rotation paraboloid with the axis of symmetry perpendicular to the sample surface it turns out

$$V(d) = -\frac{2A_{\mathrm{H}}}{(n-2)(n-3)} \int_{z=0}^{z=\infty} \frac{2Rzdz}{(d+z)^{n-3}} \qquad \text{for } n > 3 \tag{49}$$

$$= -\frac{4A_{\mathrm{H}}R}{(n-2)(n-3)(n-4)(n-5)\, d^{n-5}}, \tag{50}$$

where R is the apex radius of the parabola and d denotes the tip-sample distance.

For $n = 6$ (van der Waals-forces) the interaction energy is

$$\underline{\underline{V_{\mathrm{vdW}}(d) = -\frac{A_{\mathrm{H}}R}{12d}}}. \tag{51}$$

A typical value[23] for the Hamaker constant is $A_{\mathrm{H}} = 0.1\mathrm{aJ}$.

3.2.2 Electrostatic Forces between Tip and Sample

In Ref. [24] a general expression is given for the force acting on the tip due surrounding electrodes.

$$\begin{aligned} F_{\text{electrostatic}}(\mathbf{d}) \;=\; & \frac{1}{2} \sum_i \sum_{\substack{j \\ j>i}} \partial_d C_{i,j}(\mathbf{d}) \cdot \left(V_{j,i} + \frac{\triangle \mu_{j,i}^{\mathrm{ch}}}{e} \right)^2 \\ & - \sum_{\substack{i \\ i \neq t}} \partial_d Q_i(\mathbf{d}) \cdot \left(V_{i,t} + \frac{\triangle \mu_{i,t}^{\mathrm{ch}}}{e} \right) \\ & + \partial_d W_{\mathrm{ion}}(\mathbf{d}), \end{aligned} \tag{52}$$

where $\mathbf{d}$ describes the translational movements of the electrode of interest.

The first term gives the interaction force between the electrodes due to the differences in their electrostatic potentials $\Phi_j - \Phi_i = V_{j,i} + \triangle \mu_{j,i}^{\mathrm{ch}}/e$. $V_{j,i}$ is the applied voltage between two electrodes of different materials and defines the difference in the electrochemical potentials $-e \cdot V_{i,j} \equiv \mu_i^{\mathrm{elch}} - \mu_j^{\mathrm{elch}}$, where the electrochemical potential $\mu_i^{\mathrm{elch}} \equiv \mu_i^{\mathrm{ch}} - e\Phi_i$ is the difference between the chemical potential μ_i^{ch} and the electrostatic potential Φ_i of

the electrode i. As in the case of two parallel plates, these contributions are quadratic in the electrostatic potential differences and are weighted by factors describing the change of the capacitance coefficient $C_{i,j}$ between two electrodes by changing the position $\mathbf{d}$ of the electrode of interest.

The second term in Eq.52 is linear in the electrostatic potentials of the electrodes. It reflects the force caused by the total image charge Q_i induced by the presence of charges $\rho_{\text{ion}}(\mathbf{r})$ between the electrodes. The index t denotes the electrode defined as the tip.

The third term in Eq.52 is independent of the electrostatic potentials. It describes the change in the potential energy W_{ion} due to the interaction of the charge distribution $\rho_{\text{ion}}(\mathbf{r})$ between the electrodes with themselves taking into account the image charges induced by $\rho_{\text{ion}}(\mathbf{r})$ on the electrodes.

Simplifying Eq.52 for the case of a tip and one electrode (the sample surface) yields the force acting on the tip

$$\begin{aligned} F_{\text{electrostatic}}(\mathbf{d}) &= \frac{1}{2}\partial_d C_{s,t}(\mathbf{d}) \cdot \left(V_{t,s} + \frac{\triangle\mu^{\text{ch}}_{t,s}}{e}\right)^2 \\ &\quad -\partial_d Q_s(\mathbf{d}) \cdot \left(V_{s,t} + \frac{\triangle\mu^{\text{ch}}_{s,t}}{e}\right) \\ &\quad +\partial_d W_{\text{ion}}(\mathbf{d}), \end{aligned} \tag{53}$$

where the index s denotes the sample surface and t denotes the tip. Assuming that there are no charges between tip and sample Eq.53 reduces to

$$\underline{\underline{F_{\text{electrostatic}}(\mathbf{d}) = \frac{1}{2}\partial_d C_{s,t}(\mathbf{d}) \cdot \left(V_{t,s} + \frac{\triangle\mu^{\text{ch}}_{t,s}}{e}\right)^2}}, \tag{54}$$

where $C_{s,t}(\mathbf{d})$ is the capacitance coefficient between tip and sample, $V_{t,s}$ is the applied voltage between tip and sample and $\triangle\mu^{\text{ch}}_{t,s} = \mu^{\text{ch}}_t - \mu^{\text{ch}}_s$.

The force gradient of the general expression (52) is

$$\begin{aligned} \partial_d \mathrm{F}_{\text{electrostatic}}(\mathbf{d}) &= \frac{1}{2}\sum_i \sum_{\substack{j \\ j>i}} \partial_d^2 C_{i,j}(\mathbf{d}) \cdot \left(V_{j,i} + \frac{\triangle\mu^{\text{ch}}_{j,i}}{e}\right)^2 \\ &\quad -\sum_{\substack{i \\ i\neq t}} \partial_d^2 Q_i(\mathbf{d}) \cdot \left(V_{i,t} + \frac{\triangle\mu^{\text{ch}}_{i,t}}{e}\right) \\ &\quad +\partial_d^2 W_{\text{ion}}(\mathbf{d}). \end{aligned} \tag{55}$$

Reducing the expression for a tip-sample system and assuming that no charges are present between tip and sample the force gradient becomes

$$\underline{\underline{\partial_d F_{\text{electrostatic}}(\mathbf{d}) = \frac{1}{2}\partial_d^2 C_{s,t}(\mathbf{d}) \cdot \left(V_{t,s} + \frac{\triangle\mu^{\text{ch}}_{t,s}}{e}\right)^2}}. \tag{56}$$

Explicit calculations of the electrostatic forces between tip and sample are shown in Ref.[28], several analytic models and their degree of validity are discussed there. They

calculated the electrostatic force acting on a tip using the image method of equipotentials under the assumption of a conductive tip in front of a conductive plane and no charges between tip and plane. The tip was assumed to be of the shape as sketched in Fig.33. In the table below the analytic expressions are listed for different models. For small tip-sample distances ($d < R$) the model calculation based on a sphere in front of the surface of the sample and for large tip-sample distances ($d > L \gg R$) a tip model as drawn in Fig.33 was employed.

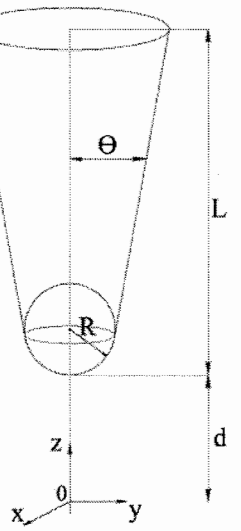

Figure 33: Geometrical characteristics of the model used for the tip. For small distances ($d < R$) the tip can be approximated by a sphere with radius R seperated at a distance d from the sample surface.

	Small tip-sample distance ($d < R$)	Large tip-sample distance ($d > L \gg R$)
Model	Sphere	Modified sphere
Expression of the force $\mathrm{F}_{\mathrm{electrostatic}}$	$-\pi\epsilon_0 \left(V_{t,s} + \frac{\triangle\mu^{\mathrm{ch}}_{t,s}}{e}\right)^2 \frac{R}{d}$	$-\pi\epsilon_0 \left(V_{t,s} + \frac{\triangle\mu^{\mathrm{ch}}_{t,s}}{e}\right)^2 \left(\frac{L}{2d} s\left(\theta\right)\right)^2$
Gradient of the force $\partial_d \mathrm{F}_{\mathrm{electrostatic}}$	$\propto \frac{1}{d^2}$	$\propto \frac{1}{d^3}$
Localization of the force on the tip	Apex	not localized

where $s\left(\theta\right) = a\theta + b$ is a semi-empirical factor with values $a = 0.13$ and $b = 0.72$ for $5 < \theta < 50$.

3.2.3 Capillary Force

As discussed in section 1.3, part I, surfaces are covered with a water film at room temperature and room pressure as long as they are not hydrophobic. To compute the interaction force between tip and sample a model of a sphere and a flat surface is employed. Fig.34b shows a macroscopic sphere at a distance d away from the sample surface and a liquid bridge is established in between the sphere and sample. A derivation considering the

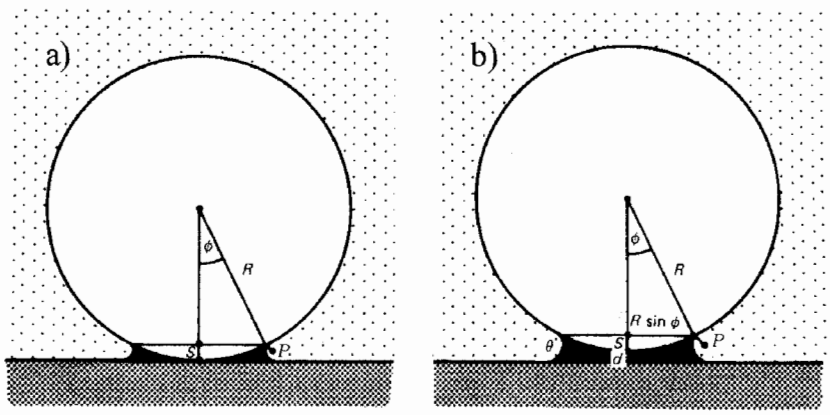

Figure 34: The left figure shows a sphere touching a liquid coated surface and the drawing on the right shows the sphere in a distance d away from the surface, but the sphere is still in contact with the liquid.

Laplace pressure in the liquid[25] and under the assumption that the angle ϕ is small, the attractive force between a sphere and the surface due to the presence of a liquid bridge is [23]

$$F_{\text{capilar}} = -\frac{4\pi R\gamma_L \cos\theta}{1+\frac{d}{s}}, \tag{57}$$

where γ_L is the surface energy of the liquid, R is the radius of the sphere, d the tip-sample distance and s is defined in Fig.34a. θ corresponds to the angle between the sample surface, the point on the sample surface placed directly under the sphere and point P in Fig.34. The additional force arising from the resolved surface tension around the circumference is always small compared to the Laplace pressure contribution, except for $\theta \approx 90\,°$[23].

An estimation using the equations (51) and (57) shows that the van der Waals force is negligeable if a water film is present. The van der Waals interaction force is

$$F_{\text{vdW}}(d) = -\frac{A_{\text{H}}R}{6d^2} \approx -\frac{0.1\times10^{-18}\,\text{J}}{6}\frac{R}{d^2} \approx -10^{-20}\,\text{J}\,\frac{R}{d^2}, \tag{58}$$

where $A_{\text{H}} = 0.1\text{aJ}$ is the Hamaker constant. An estimation for the capillary force is obtained by using the definitions in Fig.34 and Pythagoras' theorem $s^2 \approx (2R\sin(\phi/2))^2 +$

$(R\phi)^2 \approx 2R^2\phi^2$:

$$
\begin{aligned}
F_{\text{capilar}} &= -\frac{4\pi R\gamma_L \cos\theta}{1+\frac{d}{s}} && (59)\\
&\approx -\frac{4\pi R\gamma_L \cos\theta}{1+\frac{d}{\sqrt{2}R\phi}} && (60)\\
&\approx -4\pi R\gamma_L \cos\theta \qquad \text{for } R\phi \approx R\sin\phi \gg d && (61)\\
&= -4\pi \cdot 7.3\times 10^{-2}\,\mathrm{J\,m^{-2}} \cdot R\cos\theta && (62)\\
&\approx -R\cos\theta \cdot 1\,\mathrm{J\,m^{-2}}\,. && (63)
\end{aligned}
$$

where $\gamma_L = 73\,\mathrm{mJ\,m^{-2}}$ is the surface energy of water [23]. The simplification for the capillary force using $R\phi \approx R\sin\phi \gg d$ is fulfilled for blunt tips ($R \gtrsim 50\,\mathrm{nm}$) and a water film of a thickness of about 10 nm, limiting the maximal tip-sample distance to about 20 nm, where the tip is in contact with the sample due to a water bridge and F_{capilar} is applicable. The assumption of blunt tips is unfortunately justified by the tip crashes occurring during the measurement procedure as shown in section 1, part V.

Comparing Eq.58 and Eq.59 and setting $\cos\theta = 1$ shows us that the capillary force dominates the van der Waals force down to distances of the order of Ångstroms:

$$
F_{\text{vdW}}(d) = F_{\text{capilar}} \Longrightarrow -10^{-20}\,\mathrm{J}\cdot\frac{R}{d^2} \approx -R\cdot 1\,\mathrm{J\,m^{-2}} \Longrightarrow d \approx 10^{-10}\,\mathrm{m}\,. \qquad (64)
$$

At distances of angstroms the repulsive forces of the Lennard-Jones potential are dominant, therefore we neglect the influence of the van der Waals force if a waterfilm is present.

4 Discussion of the Measurements

In this section we discuss the measurements presented in section 1. The physical essence of our measurements is extracted using the relations obtained in section 2 and the subsequent discussion is based on section 3.2.

The measurements are obtained by using a fork oscillating with an amplitude of about 10 nm. We are not able to control the amplitude of the oscillation, i.e. if the amplitude decreases while approaching the tip closely to the sample surface the stimulating voltage could not be raised, such that the amplitude remains constant. Therefore we have to bear in mind that close to the surface the measured frequency shift $\triangle f$ can be lower than the true value.

Because the oscillation amplitude of the fork was about 10 nm which is of the order of the tip-sample distance we apply expression (41)

$$\left.\frac{\triangle f}{f_0}\right|_{\text{asymm}} \cong -\frac{1}{\sqrt{2}\pi}\frac{1}{(k_{\text{a}}+k_{\text{c}})\,A^{3/2}}\frac{nC_{\text{n}}}{D^{n+1/2}}I_1\,(n+1)\,,$$

obtained by the perturbation theory for inverse power law potentials (38)

$$V_{\text{ts}}\,(z) = -\frac{C_{\text{n}}}{z^n}$$

We are not able to calculate the potential exactly, because we were not able to record the amplitude of the tuning fork while measuring. But we can determine the power law of the interacting potential by plotting the logarithm of the normalized frequency-shift $\triangle f/f_0$ versus the logarithm of the tip-sample distance. In a double logarithmic plot the slope of the curve corresponds to the exponent in the inverse power law of the interacting potential:

$$(41) \Longrightarrow \left.\frac{\triangle f}{f_0}\right|_{\text{asymm}} \sim \frac{1}{D^{n+1/2}} \tag{65}$$

$$\Longrightarrow \log\left(\left.\frac{\triangle f}{f_0}\right|_{\text{asymm}}\right) = -\left(n+\frac{1}{2}\right)\cdot\log\left(\frac{D}{1\,\text{nm}}\right) + \text{const.}$$

$$\Longrightarrow n \Longrightarrow V_{\text{ts}}\,(z) \sim \frac{1}{z^n} \tag{66}$$

4.1 Gold Surface and Platinum-Iridium Tip

- Calibration of the zero point

  While measuring we intend to avoid any contact of the tip with the surface, therefore we never know where the surface really is. We like to define the zero point of the z-axis to be placed on the sample surface. The only possibility to determine the zero point of the z-axis is to observe the distance dependent behavior of the frequency-shift $\triangle f$.

  The plot of the investigation of the Gold surface by a Platinum/Iridium tip (Fig.28) shows a frequency shift $\triangle f$ with a steep slope at smaller tip-sample separations.

This behavior of $\triangle f$ can be explained by the repulsive term in the Lennard-Jones potential[21] $V_{\text{ts}} \sim z^{-n}|_{n=12}$ remembering that $\triangle f \sim D^{-(n+1/2)}$. Thus we maintain that the $\triangle f$ curve approaches asymptotically the zero point corresponding to the sample surface. Following the argument above we defined the coordinate system in Fig.28.

- Discussion

  We discuss the three regions inscribed in Fig.28 separately.

  - Region I

    There is no frequency shift, thus there is no tip-sample interaction force acting on the tip.

  - Region II

    The steep slope of the curve between 0 nm and 2 nm is due to the repulsion of the ion cores of the Gold and Platinum or Iridium atoms, respectively.

    At the minimum at 2 nm the attractive forces become dominant. In section 3.2.3, we estimated (Eq.64) that the capillary force dominates the van der Waals force, which is expected to be the force of the longest range besides the electrostatic force (Sec.3.2.2). Since the Gold surface and the tip are covered with a water film at room temperature (Sec.1.3) we maintain that the attractive force reaching up to 20 nm is due to the capillary force. The water bridge between tip and sample breaks at a tip-sample distance of 20 nm .

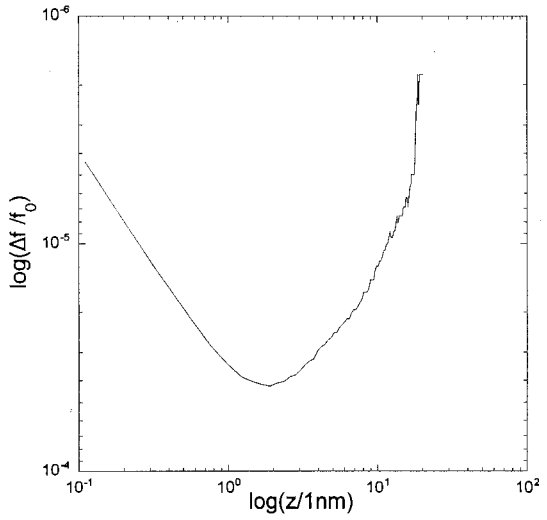

Figure 35: Double logarithmic plot of the normalized frequency-shift $\triangle f/f_0$ versus normalized distance. The frequency shift of the tuning fork due to the distance dependent interaction between a Platinum/Iridium-tip and a Gold surface was investigated.

For a closer look at the characteristics of the interaction forces we employ Fig.35 that shows a plot of the negative logarithm of the relative frequency shift $\triangle f/f_0$ versus the logarithm of the normalized tip-sample distance. In

Fig.35 only region II of Fig.28 is plotted, because $\triangle f$ equals zero in region I and the logarithm diverges.

The measurement starts at the smallest separation between tip and sample and then the tip is pulled back away from the surface. First the tip feels an exponentially decaying repulsive force until the minimum value at 2 nm is reached.

The attractive part of the curve between 2 nm and 20 nm shows three different regions. The curve segment in the first region between 2.5 nm and 8.5 nm has a slope of 0.74 corresponding to $n \approx 0.24$, the segment in the second region between 8.5 nm and 15.6 nm has a slope of 1.43 corresponding to $n \approx 0.93$ and in the third section the slope is very steep with a value of about 8.5 corresponding to $n \approx 8$.

As mentioned we maintain that the attractive interaction between tip and sample is caused by a waterfilm on tip and sample surface. Because of the occurrence of numerous tip crashes (section 1, part V) the soft Platinum/Iridium tip is flat and broad (≈ 100 nm diameter at the front). In the region between 2.5 and 8.5 nm the tip is immersed in the water film such that the tip-sample distance is less than or equal to the thickness of the water film and the only contribution to the force comes from the surface tension on the side of the tip. Then the tip is pulled back until the tip-sample distance of 15.6 nm is reached, which corresponds to about twice the thickness of the waterfilm. In this region the shape of the front of the tip becomes important. By pulling the tip further away the water film on the tip and the water film on the sample are still in contact, but the water bridge between tip and sample is stretched more and more until the bridge breaks at 20.5 nm. Under the assumption that the water films on the tip and on the sample surface are of the same thickness we conclude that the water film is about 8 nm thick.

– Region III

Region is III is not accessible by measurement.

4.2 Graphite Surface and Tungsten Tip

- Calibration of the zero point

Fig.29 shows no steep increasing of the frequency shift $\triangle f$ by approaching the tip towards the sample in region III as observed in section 4.1. We explain the linear slope in region III as follows. We know that HPOG consists of carbon layers that are bound weakly together and therefore the material reacts like a soft medium if a hard object is pressed perpendicular on the HPOG surface. By approaching the very hard tungsten tip close to the HPOG surface the carbon layers give way and the tip is able to penetrate the surface. As zero point of the coordinate system we like to define the point where the sample surface was before any interaction with the tip occurred. But because the tip is our only sensor to determine the properties of the sample we have to extract the approximate zero point out of our measurements.

The first attempt is to look at the curves in Fig.29 and define the zero point in the region where $\triangle f$ starts to increase linearly. This transition is observed between

7 and 9 nm on the former coordinate system. This attempt fails because $\triangle f$ is negative for all curves in this region, but the pushing away of the HPOG layers must result in an repulsive force between tip and sample, i.e. the $\triangle f$ has to be positive if no voltage is applied.

The second attempt to define the zero point is to set it at the transition point where the sign of the 0 V-curve in Fig.29 changes, i.e. where the attractive force turns into a repulsive force. This is a reasonable approximation, but the sample surface is expected to be more far away from the tip, because the repulsive potential is of finite range.

We decided to apply a third method. We look at the long range behavior of the $\triangle f$ curves in Fig.29. The 0 V-curve tells us that the fork is not influenced by any force in region I, i.e. far away from the sample. The nonzero voltage measurements in Fig.29 show nonzero $\triangle f$-values in region I. Thus we know that the shift of the frequency in region I of Fig.29 is only due to electrostatic tip-sample interactions. Therefore we plot the $\triangle f$ measurements in a double logarithmic plot and compare them with theory by using the relations (66). To achieve the pure electrostatic interaction we subtracted the zero voltage measurement from the nonzero voltage measurements in Fig.29. As an example we have chosen the -7 V-curve and we

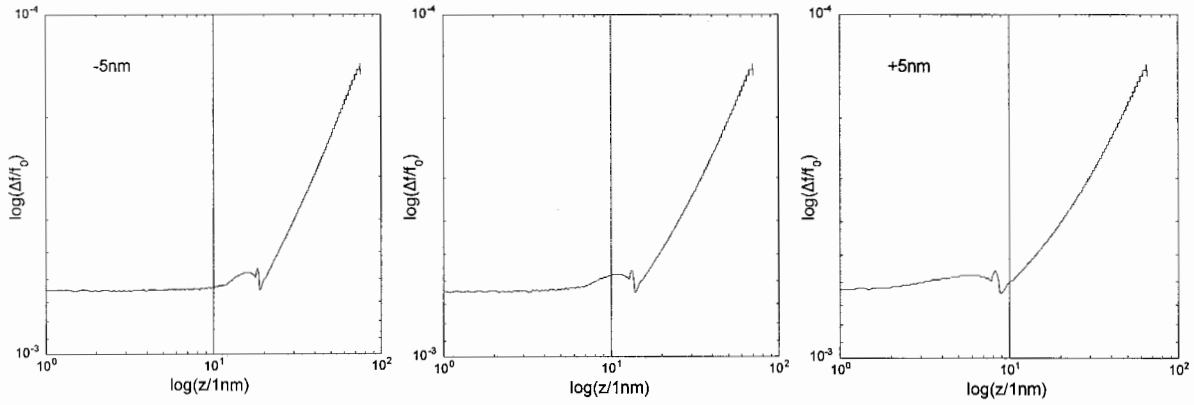

Figure 36: Double logarithmic plots of the normalized frequency-shift $\triangle f/f_0$ versus normalized distance. The curve has been recorded while applying a voltage of -7 V between tip and sample. The background was subtracted to achieve the pure electrostatic interaction. On the plot on the left the zero point is translated 5 nm away from the tip and on the plot on the right side the zero point is translated 5 nm towards the tip. The slope on the left plot is steeper than 1, the slope of the curve in the middle equals 1 and the slope of the curve on the right is less than 1.

plotted the logarithm of the negative relative frequency shift versus the logarithm of three different choices of the normalized tip-sample distance in Fig.36. From the table on page 42 we expected $n = 1$ for large tip-sample distances resulting in a slope of $n + 1/2 = 3/2$. But in Fig.36 the values of slopes vary about 0.2 around the value 1.0 of the slope in the plot in the middle. The variation in slope is very small compared with the translation of the zero point. We translated the zero point of the coordinate system 5 nm away from the tip in the left plot and 5 nm towards the tip in the plot on the right. To achieve a slope of 3/2 as expected from the

model calculations for large tip-sample distances a translation of the zero point of more than 20 nm away from the tip is necessary, resulting in an unrealistic action range of more than 25 nm for the repulsive forces. In Ref.[28, Fig. 6] is shown that for intermediate distances (tip dimension $\sim$ tip-sample distance) $n = 1/2$, resulting in a slope of 1, is reasonable and therefore we treat the choice for the zero point inscribed in the plot in the middle of Fig.36 as the correct gauge. Fig.29, 30 and 31 are already plotted in the correct coordinates.

- Discussion of the zero voltage measurement

  We discuss the three regions inscribed in Fig.28 separately.

  - Region I

    No frequency shift occurs, thus no tip-sample interaction exists.

  - Region II

    As discussed in section 3.2.3 we estimated (Eq.64) that the capillary force dominates all interactions with the exception of the electrostatic force (Sec.3.2.2). The measurement was taken while approaching the tip towards the sample. At a tip-sample distance of 14 nm the water film covering the tip touches the water film covering the surface and immediately the water is pulled in between the tip and sample in favor of minimization of its surface energy. This immediate establishing of the capillary force results in an sudden drop of $\triangle f$. Because this effect starts at 14 nm the thickness of the waterfilm on the sample can be estimated to be 7 nm, assuming that tip and sample are both coated by a film of the same thickness.

    By further approaching the tip to the sample a minimum at 11 nm is passed and then a linear increase of $\triangle f$ occurs. The reason for this behavior was discussed above (Calibration of the zero point).

  - Region III

    The linear increase of $\triangle f$ continues while approaching.

- Discussion of the nonzero voltage measurements

  - Region I

    Fig.37 shows the negative logarithm of the normalized frequency-shift of the $-7\,\mathrm{V}$, $-5\,\mathrm{V}$ and $-3\,\mathrm{V}$ measurements plotted versus the logarithm of the normalized tip-sample distance. The $0V$-measurement was subtracted from the data of the nonzero voltage measurements to achieve the pure electrostatic interaction. This is reasonable under the assumption that the individual forces are additive[23].

    All curves are parallel with a slope of 1 resulting in an exponent $n = 1/2$ in the inverse power law interaction potential (66).

  - Region II

    All curves in Fig.37 are constant and parallel. This is because water is a highly dielectric medium with $\varepsilon_{H_2O} = 81.1$ at $18\,^{\circ}\mathrm{C}$[26] compared to vacuum or air ($\epsilon = 1$). Therefore the interaction treats the surface of the water film like

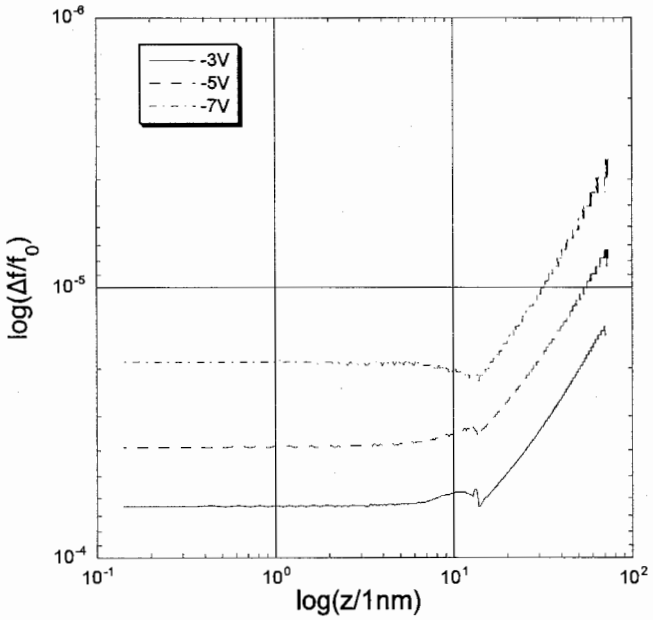

Figure 37: Double logarithmic plot of the normalized frequency-shift $\triangle f/f_0$ versus normalized distance. The measurement with $0V$ applied was subtracted to achieve the pure electrostatic interaction.

a metallic surface and everywhere on and inside the "metallic" medium the potential remains constant.

The little structures of the curves in Fig.37 at the transition point from region I to region II are due to the processing of the curves and of no physical relevance. The structure of the $-7\,\mathrm{V}$ curve is due to the limited measuring resolution (Sec.1.2)

– Region III

The same considerations are valid as in region II, but region III could not be plotted in Fig.37 because the logarithm of negative z-values diverges.

- Discussion of the frequency shift depending on the applied voltage at fixed distances

Fig.30b shows the behavior of the frequency shift at fixed tip-sample distances while changing the tip-sample potential difference. In Fig.30a we have chosen four fixed values of the tip-sample distance z, two inside and two outside the range of the water bridge between tip and sample. The same data as used in Fig.29 are now plotted in Fig.30b versus the applied voltage.

For the discussion we make use of Eq.43

$$\left.\frac{\triangle f}{f_0}\right|_{\text{asymm}} \cong \frac{1}{2\left(k_{\text{a}}+k_{\text{c}}\right)} \left.\frac{\partial^2 V_{\text{ts}}(z)}{\partial z^2}\right|_{z=D} \cdot \frac{\sqrt{2}}{n\left(n+1\right)\pi} \left(\frac{D}{A}\right)^{3/2},$$

which is equivalent to the relation (41) used above. For the discussion of the curves in Fig.30b, where the tip-sample distance is constant for each curve the relation

above can be simplified

$$\left.\frac{\triangle f}{f_0}\right|_{\text{asymm}} \sim \left.\frac{\partial^2 V_{\text{ts}}(z)}{\partial z^2}\right|_{z=D}, \tag{67}$$

where we assume that the amplitude of the oscillation of the fork is constant at constant tip-sample separation. According to Eq.67 the frequency shift $\triangle f$ is proportional to the force gradient.

Assuming that there are no charges between tip and sample the force gradient is (Eq.56)

$$\partial_d F_{\text{electrostatic}}(\mathbf{d}) = \frac{1}{2}\partial_d^2 C_{s,t}(\mathbf{d}) \cdot \left(V_{t,s} + \frac{\triangle \mu_{t,s}^{\text{ch}}}{e}\right)^2 \tag{68}$$

where $C_{s,t}(\mathbf{d})$ is the capacitance coefficient between tip and sample, $V_{t,s}$ is the applied voltage between tip and sample and $\triangle \mu_{t,s}^{\text{ch}} = \mu_t^{\text{ch}} - \mu_s^{\text{ch}}$ is the difference of the chemical potentials. Because $C_{s,t}(\mathbf{d})$ does not depend on the applied voltage the force gradient in Eq.68 is proportional to the frequency shift in Eq.67

$$\partial_d F_{\text{electrostatic}}(\mathbf{d}) \sim \left(V_{t,s} + \frac{\triangle \mu_{t,s}^{\text{ch}}}{e}\right)^2 \sim \left.\frac{\triangle f}{f_0}\right|_{\text{asymm}}. \tag{69}$$

Eq.69 explains the parabolic behavior of $\triangle f$ versus applied voltage. Because the electrostatic interaction is attractive the aperture of parabolas points towards negative $\triangle f$ values. Eq.69 describes a parabola with the apex shifted by the value of $\triangle \mu_{t,s}^{\text{ch}}/e$ from $0\,\text{V}$. Using the difference of the photoelectric work function[27] of tungsten ($4.55\,\text{eV}$) and HPOG ($4.8\,\text{eV}$) we predict that the shift must be of the value $4.55\,\text{V} - 4.8\,\text{V} = -0.25\,\text{V}$ and the apex of the parabola should be placed at $0.25\,\text{V}$. Looking at Fig.30b the prediction is in agreement with our measurement, the parabolas are shifted by $0.2 - 0.4\,\text{V}$ towards positive voltages.

The different apex radii of the $\triangle f$ curves at different tip-sample distances are caused by the dependence of the capacitance coefficient $C_{s,t}(\mathbf{d})$ on the distance.

5 Increasing the Resolution of the Measurement

First the resolution of the force-distance measurements was not satisfying. We have a fixed amount of 2^{12} bits available to cover the measurement range. The usual working range (approach, topography imaging) expands over a z-range of 4.722 μm, i.e. the resolution is 11.5 bit per 10 nm. Doing force-distance measurements we need only a maximal range of the order of 100 nm, but we need a higher resolution in z-direction. Therefore we reduce the maximal z-range and we spread the 2^{12} bits over the new z-range and obtain a higher resolution.

Because of the reduction of freedom of movement we have to drive the tip to the starting point of the measurement by an additional dc voltage source. Fig.38 shows how the external offset voltage is added to the reduced internal driving signal. The reduction of the z-range is obtained by a variable voltage divider, and the external driving mechanism to control the coarse tip movements is added by leading the internal signal through a Yokogawa dc-source. The division of the voltage input to the piezo tube can

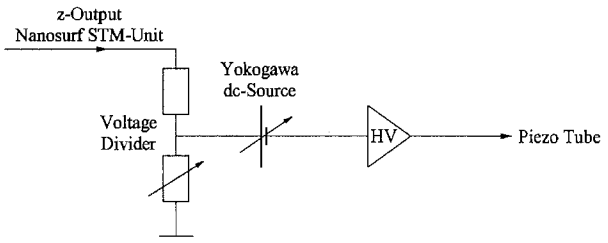

Figure 38: Schematic drawing a voltage divider followed by a dc-sourcethat adds voltage to the former signal.

be chosen from 2^{-2} to 2^{-8}. The setting of 2^{-2} corresponds to the common working range of $\pm 2.361\,\mu$m (the value of $2^{-2} = 1/4$ is due to the division of the initial working range down to voltages that are supportable by the piezo tube as discussed in section 1.4.2, part I). Dividing the driving voltage down by the factor 2^{-3} doubles the resolution and dividing further down increases the resolution more and more. Dividing further down than by the factor 2^{-5} is not reasonable, because the recording resolution is of the order of Ångstroms, which is below the accessible resolution of the SFM. The division factors and the corresponding maximal z-ranges are shown in the table below. In the last column the resulting resolution is calculated.

Setting of the voltage divider	Maximal z-range	Resolution [bits/10 nm]
2^{-2}	4.722 μm	11.5
2^{-3}	1.918 μm	21.4
2^{-4}	0.9 μm	45.5
2^{-5}	0.466 μm	87.9

Part IV
Topographic Imaging in Dynamic Mode

Fig.39 shows pictures of an antidot lattice at different scales. The exact steps and data to obtain these scans are listed in the appendix "*Bedienungsanleitung für selbstgebautes SFM HPF C17*". The pictures on the left show the frequency-shift $\triangle f$ recorded while scanning the surface. The pictures on the right side show the z-voltage output to the piezo tube that corresponds to the movement of the tip reacting on the $\triangle f$-signal.

The upper row of the pictures shows the whole antidot lattice placed on a hall bar in an area of $8.03\,\mu\text{m} \times 7.96\,\mu\text{m}$. The row in the middle shows a part of the lattice in an area of $303\,\mu\text{m} \times 303\,\mu\text{m}$. The doughnut-like structure of the antidots can be recognized very well. On the lower two pictures four antidots are depicted in an area of $0.724\,\mu\text{m} \times 0.724\,\mu\text{m}$. The periodic structure between the antidots is not real. The virtual structures are caused by a double tip due to a tip crash after taking the second picture. The tip crash occurred because the electronics broke down, but the reason for that has been found and eliminated. Fig.39 tells us that structures of the dimension of 20 nm can be distinguished from each other.

The quality of the pictures on the right side is not as good as the quality of the pictures of the frequency-shift, indicating that the parameter of the z-feedback loop cannot be set as accurate as desired. The pictures show diagonal lines arising from a hopping of the signal every second. Obviously this is a virtual structure caused by the z-feedback loop. The disadvantageous features mentioned above are discussed in part V.

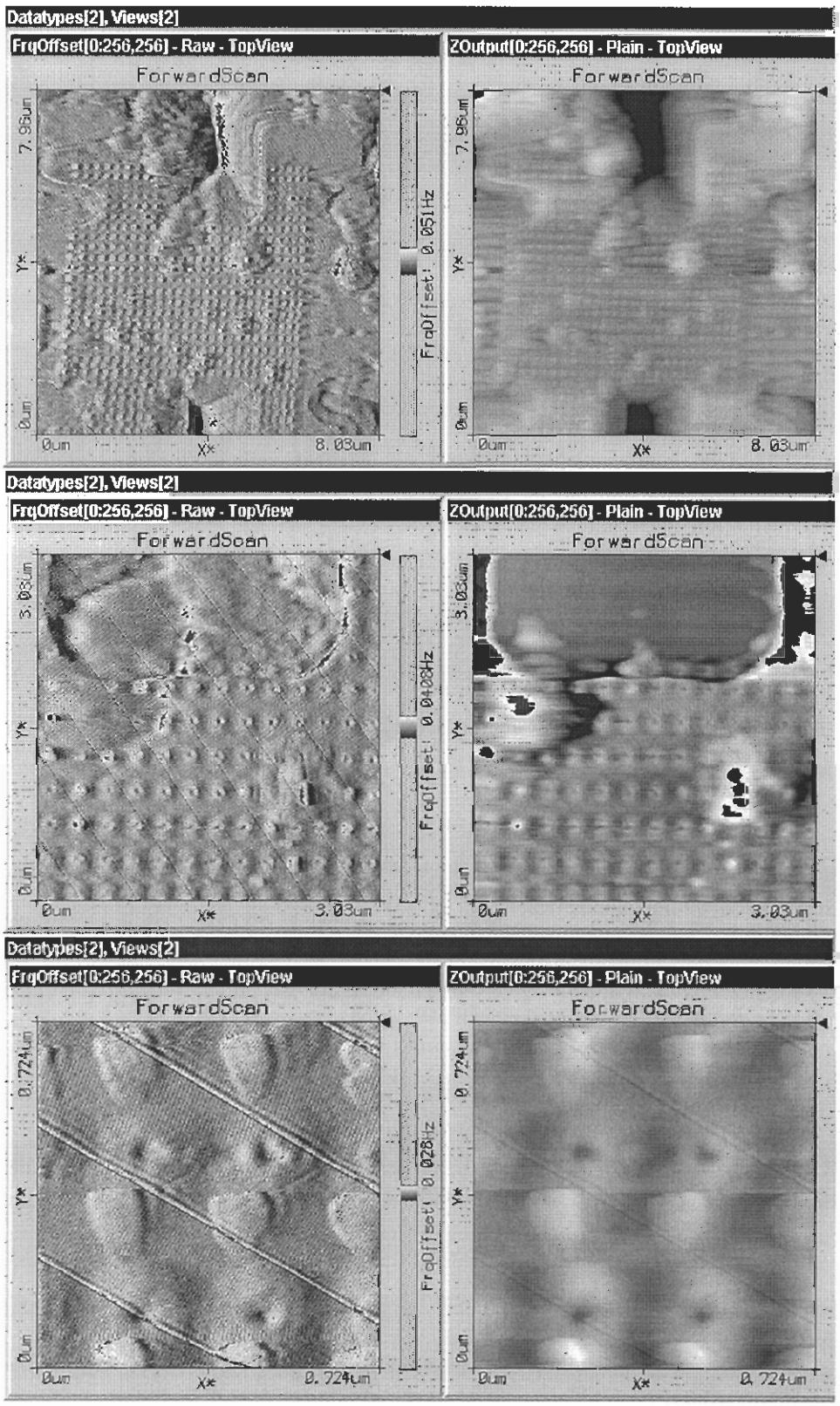

Figure 39: Pictures of an antidot lattice. On the left side the frequency shift is shown and on the right side the corresponding z-signal. The picture on the top shows the lattice placed on a hall bar. The lower pictures show enlarged parts of the picture on the top.

Part V
Outlook

1 Suggestions to improve the SFM

1.1 Software

- There are some mistakes of programming in the implemented package to measure the force-distance curves as shown in Fig.40. In Fig.40 the elongation of the piezo tube versus time is recorded by a x-y-plotter. The force-distance measurements are taken in region III. The only difference of Fig.40a and Fig.40b is that in the former the tip sweeps from the surface away and in the latter the tip is swept towards the surface. In region I the z-feedback is locked. In region II the z-feedback is switched off and the tip should be moved to the starting point of the measurement. Obviously the sign is mixed up in Fig.40b and the tip is moved in the wrong direction, probably into the surface. In Fig.40a the movement is in the correct direction, but the end point does not coincide with the starting point of the measurement ramp at $t = 0\,\mathrm{s}$. Region III is the measurement ramp. In region IV the tip should move back so that the z-feedback can be enabled. The sign of the movements are mixed up again and in both plots the tip is driven into the surface at $t = 8\,\mathrm{s}$. In region V the z-feedback is locked. The tip in region V is closer to the surface than the tip was in region I due to the creep of the piezo tube. To sum up, this procedure destroys the tips and therefore the achieved results are not reliable.

  In the measuring routine we have only the choice of sweeping towards the surface or sweeping away from the surface. Desirable is that during a single measurement process the tip sweeps towards the surface and back to the starting position, because it is important to know the hysteretic behavior of the measurement.

  To achieve reliable force-distance measurements the sweeping of the ramp has to be slower than the limit of 1 minute.

  Concluding, the force-distance measurement routine is not at all satisfactory. Until the mistakes are not corrected the measurement should be done by hand. The best way is to record the frequency shift while a Yokogawa dc-source sweeps the ramp.

- The pictures of the antidots in Fig.39 on page 54 indicate that the parameters of the z-feedback are not properly set, because the pictures of $\triangle f$ on the left are sharp and the pictures of the z-movement of the tip on the right are blurred although $\triangle f$ and the z-movement should be directly correlated. The proportional- and the integral-gain of the z-feedback loop can be set digitally in a range from 1 to 16. The P-gain is not sensible enough and the I-gain has to be more sensitive. To improve the performance I suggest that the steps of the P-gain should be at least twice as coarse as before and the range of the I-gain should be reduced to lie between 8 and 16.

- The pictures of the antidots in Fig.39 show an additional feature. The lines crossing the pictures are caused by a hopping of the signal. This hopping occurs periodically

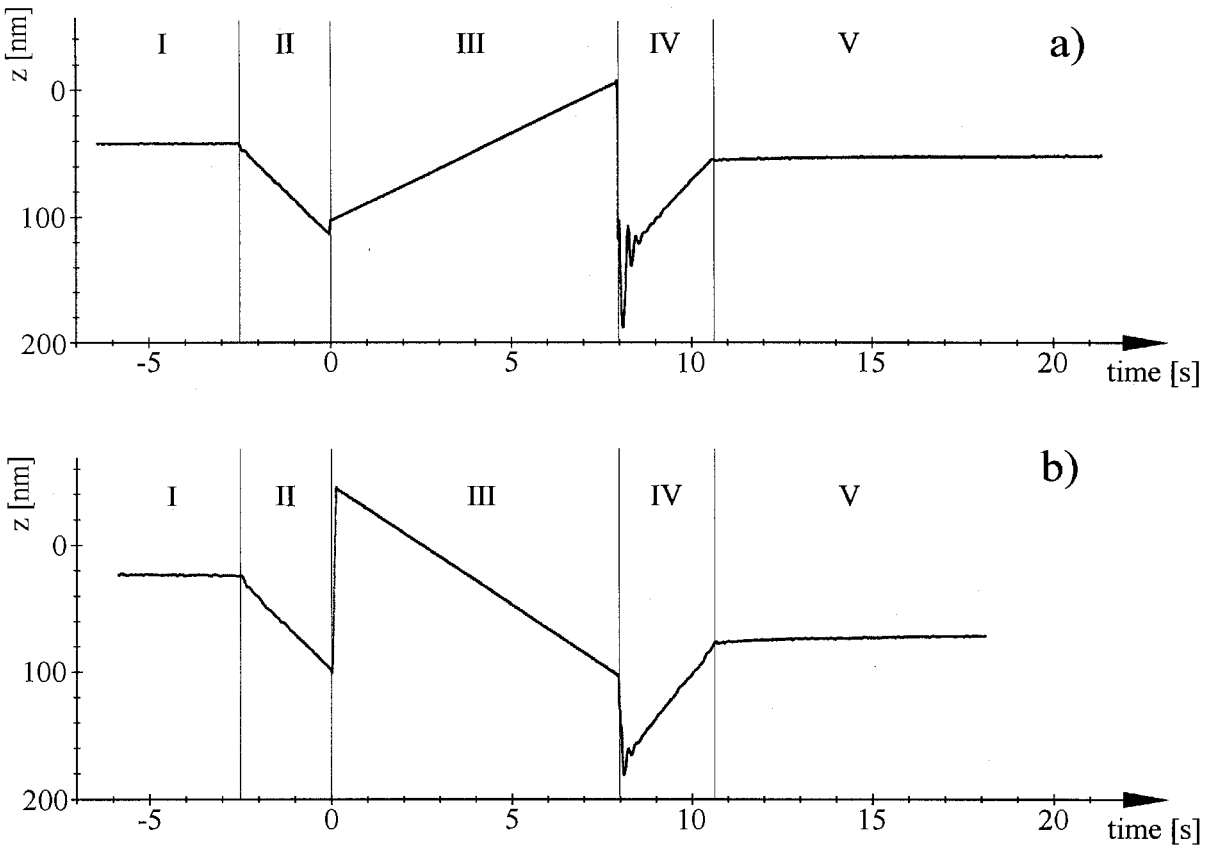

Figure 40: Measurements of the tip-sample distance during a force-distance measuring process. Plot a) shows the sweeping away of the tip from the surface in region III and b) shows the sweeping towards the surface.

with a period of 1 second. The hopping occurs only if the z-feedback is locked. If the PLL is locked and the z-feedback is not enabled the hopping does not occur. This indicates that the z-feedback is responsible for the hopping of the signal. The interfering signal is strictly periodic, indicating that the digital part of the machine is the source of this signal.

1.2 Hardware

- As mentioned in section 1.4.2 on page 11 the piezo tube elongates if the sample is heated. Often this elongation is large enough to drive the tip into the sample surface although the tip is withdrawn. The only solution is to do the coarse approach after heating the sample. But this procedure is impossible if we want to measure in vacuum, because the vacuum chamber is put over the SFM *and* the micrometer screws for the coarse approach. Therefore I suggest a step motor that is externally driven for the coarse approach. It is necessary that the tip can be withdrawn far enough to prevent any risk of destroying the tip while heating.

- A drawback of our SFM is that we cannot keep the amplitude of the tuning fork

oscillation constant. To achieve reliable force-distance measurements that can be interpreted properly we have to be able to keep the amplitude constant or to know how large the amplitude really is while measuring. A solution is to implement a loop that measures the current output of the fork and controls the amplitude of the stimulation of the fork such that the output current is constant.

- As seen in section 2, part III, it is important for the force-distance measurements to work with amplitudes as small as possible. To achieve small amplitudes we have to suppress noise in the signal in- and output of the tuning fork. This can be done by shorten the cables between fork and electronics and by shielding the wires at the puck where the fork is mounted.

2 Measurements

- After improving the force-distance measurement routine of the SFM the force-distance measurements in part III section 1 should be repeated again to obtain more accurate and reliable results.

- It is interesting to estimate the thickness of the film of water that coats a surface. I suggest to measure force-distance curves depending of the surrounding humidity. Therefore a humidity detector has to be installed inside the vacuum chamber. Additionally one has to investigate how humity influences the properties of the fork.

- The high spring constant makes the tuning fork ideal for lithography, where structures are oxidized locally on metals or semiconductors like titanium or GaAs by applying voltage between tip and sample.

Part VI
Appendix

1 Computations

Correlation between the Frequency Shift $\triangle f$ and the Interacting Potential

To compute the correlation between the frequency shift $\triangle f$ and the interacting potential we apply perturbation theory.

The tuning fork oscillator is modelled with the equations

$$\begin{aligned} m_1\ddot{x}_1 + k_a x_1 + \tfrac{1}{2}k_c\,(x_1 - x_2) &= 0 \\ m_2\ddot{x}_2 + k_a x_2 + \tfrac{1}{2}k_c\,(x_2 - x_1) &= 0, \end{aligned} \tag{70}$$

where m_1 and m_2 are the effective masses of the upper and lower arm of the tuning fork, respectively. The coupling between the two arms is described by k_c and the spring constant of one single arm is k_a. Defining the matrices

$$M = \begin{pmatrix} m_1 & 0 \\ 0 & m_2 \end{pmatrix}, \quad K = \begin{pmatrix} k_a + \frac{k_c}{2} & -\frac{k_c}{2} \\ -\frac{k_c}{2} & k_a + \frac{k_c}{2} \end{pmatrix}, \quad x = \begin{pmatrix} x_1 \\ x_2 \end{pmatrix} \tag{71}$$

the equations above can be written in matrix notation as

$$M\ddot{x} + Kx = 0 \tag{72}$$

The kinetic and potential energy of the system is then

$$T = \frac{1}{2}\dot{x}M\dot{x}, \qquad V = \frac{1}{2}xKx. \tag{73}$$

We now introduce the vector y with the components $y_i = \sqrt{m_i}x_i$. The kinetic and potential energies then become

$$T = \frac{1}{2}\dot{y}\dot{y}, \qquad V = \frac{1}{2}yWy \tag{74}$$

where

$$W = \begin{pmatrix} \left(k_a + \frac{k_c}{2}\right)\frac{1}{m_1} & -\frac{k_c}{2}\frac{1}{\sqrt{m_1 m_2}} \\ -\frac{k_c}{2}\frac{1}{\sqrt{m_1 m_2}} & \left(k_a + \frac{k_c}{2}\right)\frac{1}{m_2} \end{pmatrix}. \tag{75}$$

We find the Eigenmodes and the Eigenfrequencies of the system (i.e. the matrix W)

$$\Omega_{1,2}^2 = \left(k_a + \frac{k_c}{2}\right)\frac{m_1 + m_2}{2m_1 m_2} \pm \sqrt{\left(k_a + \frac{k_c}{2}\right)^2 \left(\frac{m_1 - m_2}{2m_1 m_2}\right)^2 + \frac{k_c}{4m_1 m_2}} \tag{76}$$

and

$$e_1 = \begin{pmatrix} e_{11} \\ e_{12} \end{pmatrix}, \qquad e_2 = \begin{pmatrix} e_{21} \\ e_{22} \end{pmatrix} \tag{77}$$

with

$$\begin{array}{ll} \frac{e_{12}}{e_{11}} = \kappa + \sqrt{1+\kappa^2} \equiv h & e_{11}^2 + e_{12}^2 = 1 \\ \frac{e_{22}}{e_{21}} = \kappa - \sqrt{1+\kappa^2} \equiv -\frac{1}{h} & e_{21}^2 + e_{22}^2 = 1, \end{array} \tag{78}$$

where

$$\kappa \equiv \frac{k_a + \frac{k_c}{2}}{\frac{k_c}{2}} \frac{m_1 - m_2}{2\sqrt{m_1 m_2}}. \tag{79}$$

It follows from these relations that

$$e_{11} = e_{22} = \sqrt{\frac{1}{1+h^2}} \qquad \text{and} \qquad e_{12} = -e_{21} = \sqrt{\frac{h^2}{1+h^2}}. \tag{80}$$

The physical relevance of κ is discussed in the following. Assuming that $m_1 = m$ and $m_2 = m + \triangle m$ with $\triangle m/m \ll 1$ we find

$$\underline{\underline{\kappa \approx \frac{\triangle m/m}{k_c/k_a}}}, \tag{81}$$

i.e. κ is the ratio of the relative mass asymmetry of the two tuning fork arms and the relative coupling strength of the two arms. For very light tips and strong coupling we can assume $|\kappa| \ll 1$ and the normal modes are symmetric and asymmetric. For the opposite case of weak coupling and strong asymmetry in the masses we find $|\kappa| \gg 1$ and we obtain modes where only one of the arms oscillates while the other one is practically at rest.

We now transfer the system to normal coordinates q_i using

$$q_1 = y_1 e_{11} + y_2 e_{21} \tag{82}$$

$$q_2 = y_1 e_{12} + y_2 e_{22} \tag{83}$$

The Lagrange function in normal coordinates is

$$L(\dot{q}_1, \dot{q}_2, q_1, q_2) = \frac{1}{2}\dot{q}_1^2 + \frac{1}{2}\dot{q}_2^2 - \frac{1}{2}\Omega_1 q_1^2 - \frac{1}{2}\Omega_2 q_2^2 \tag{84}$$

$$H_0(p_1, p_2, q_1, q_2) = \frac{1}{2}p_1^2 + \frac{1}{2}p_2^2 + \frac{1}{2}\Omega_1 q_1^2 + \frac{1}{2}\Omega_2 q_2^2 \tag{85}$$

In normal coordinates the problem separates into two independent problems, one depending on q_1, $\dot{q}_1$ and the other depending on q_2, $\dot{q}_2$. We now use the Hamilton-Jacobi formalism. The action function S separates into two independent functions S_1, S_2 given by

$$S_i(q_i, E_i, t) = -E_i t + \int \sqrt{2E_i - \Omega_i^2 q_i^2}\, dq_i \tag{86}$$

We define the action variables

$$J_i = \frac{1}{2\pi} \oint p_i dq_i = \frac{E_i}{\Omega_i}. \tag{87}$$

Inserting the action variable into the action function yields

$$S_i\left(q_i, J_i, t\right) = -J_i\Omega_i t + \int \sqrt{2J_i\Omega_i - \Omega_i^2 q_i^2}dq_i. \tag{88}$$

The conjugate angle coordinate can now be obtained from

$$\beta_i = \frac{\partial S_i}{\partial J_i} = -\Omega_i t + \arcsin\sqrt{\frac{\Omega_i}{2J_i}}q_i. \tag{89}$$

Hence, the conjugate canonical transformation reads

$$q_i = \sqrt{\frac{2\Omega_i}{J_i}}\sin\left(\Omega_i t + \beta_i\right) \tag{90}$$

$$p_i = \sqrt{2\Omega_i J_i}\cos\left(\Omega_i t + \beta_i\right) \tag{91}$$

In the new variables the unperturbed Hamiltonian reads

$$H\left(J_1, \beta_1, J_2, \beta_2\right) = 0. \tag{92}$$

The perturbation Hamiltonian corresponds to the tip-sample interaction potential

$$H_1 = V_{\text{ts}}\left(d_0 + x_2\right) = V_{\text{ts}}\left(d_0 + \frac{y_2}{\sqrt{m_2}}\right) \overset{\text{Eq.82}}{=} V_{\text{ts}}\left(d_0 + \frac{q_1 e_{12} + q_2 e_{22}}{\sqrt{m_2}}\right), \tag{93}$$

where $d_0 + x_2$ is the actual tip-sample distance as sketched in Fig.32 on page 35. Therefore the equations of motion in the action-angle variables are

$$\frac{dJ_i}{dt} = -\frac{\partial\left(H_0 + H_1\right)}{\partial\beta_i} = -\frac{\partial V_{\text{ts}}}{\partial\beta_i} \tag{94}$$

$$\frac{d\beta_i}{dt} = \frac{\partial\left(H_0 + H_1\right)}{\partial J_i} = \frac{\partial V_{\text{ts}}}{\partial J_i} \tag{95}$$

This system of four differential equations coupling the two action-angle coordinate pairs (J_i, β_i) can in most cases not be solved analytically. Canonical perturbation theory can be employed to obtain approximate solutions. The lowest order is obtained if the action-angle coordinates are regarded as being constant and equal to their unperturbed values on the right hand side of the equation. Then the right hand sides can be expanded in a Fourier series and only the first constant terms are retained. We obtain

$$\frac{dJ_i}{dt} \approx -\left\langle\frac{\partial V_{\text{ts}}}{\partial\beta_i}\right\rangle \tag{96}$$

$$\frac{d\beta_i}{dt} \approx \left\langle\frac{\partial V_{\text{ts}}}{\partial J_i}\right\rangle, \tag{97}$$

which gives

$$\frac{dJ_i}{dt} \approx \frac{e_{i2}}{\Omega_i\sqrt{m_2}}\left\langle F_{\text{ts}}\left(d_0 + x_2\right)p_i\right\rangle = 0 \tag{98}$$

$$\frac{d\beta_i}{dt} \approx \frac{e_{i2}}{2J_i\sqrt{m_2}}\left\langle F_{\text{ts}}\left(d_0 + x_2\right)q_i\right\rangle = \frac{e_{i2}\Omega_i}{2E_i\sqrt{m_2}}\left\langle F_{\text{ts}}\left(d_0 + x_2\right)q_i\right\rangle, \tag{99}$$

where we used the definition $F_{\rm ts} = -\nabla V_{\rm ts}$. The first equation tells us that in lowest order the amplitude of the oscillation is unaltered. The second equation gives the frequency shift, since $\triangle\Omega_i = \dot{\beta}_i$ in this approximation. Thus the frequency shift is

$$\frac{\triangle\Omega_i}{\Omega_i} = \frac{\triangle f_i}{f_i} = \underline{\underline{\frac{e_{i2}}{2E_i\sqrt{m_2}} \langle F_{\rm ts}\left(d_0 + x_2\right) q_i \rangle}}, \tag{100}$$

where $f_i = \Omega_i/2\pi$ is the center frequency of the mode i.

Eq.100 is a generally valid result. Satisfying the condition $\kappa \ll 1$, i.e. $\triangle m/m \ll k_{\rm c}/k_{\rm a}$, the normal coordinates are

$$\left.\begin{array}{lll} q_1 = \sqrt{\frac{m}{2}}\left(x_1 - x_2\right), & k_1 = k_{\rm a} + k_{\rm c} & \rightarrow \text{asymmetric mode} \\ q_2 = \sqrt{\frac{m}{2}}\left(x_1 + x_2\right), & k_2 = k_{\rm a} & \rightarrow \text{symmetric mode} \end{array}\right\} \text{ for } m_1 = m_2 \equiv m \tag{101}$$

as discussed in section 2.2.1, part I, where the two modes are plotted in Fig.17. Using the maximal potential energy of a harmonic oscillator $E_i = \frac{1}{2}k_i A_i^2$, where $k_i \equiv k_{\rm a} + \frac{1}{2}k_{\rm c} \pm \frac{1}{2}k_{\rm c}$ and A_i is the amplitude of the i-th mode, the relative frequency shift for the asymmetric mode turns out

$$\frac{\triangle f_1}{f_1} = \underline{\underline{-\frac{1}{\left(k_{\rm a} + k_{\rm c}\right) A_1^2} \langle F_{\rm ts}\left(d_0 + x_2\right) x_2 \rangle \equiv \left.\frac{\triangle f}{f_0}\right|_{\rm asymm}}}, \tag{102}$$

where f_0 is the center frequency of the tuning fork. Since the tuning fork of the SFM is stimulated at its asymmetric resonance we focus now on the influence of the interacting force on the frequency shift of this mode.

Specific Application for Inverse Power Law potentials

In many cases, the potential between tip and sample can be well described by an inverse power law

$$V_{\rm ts}\left(z\right) = -\frac{C_{\rm n}}{z^n} \tag{103}$$

where $z = x_2 + d_0$ is the tip-sample distance and C_n is a characteristic constant depending on the properties of the material. The interacting force between tip and sample is obtained by $F_{\rm ts} = -\nabla_z V_{\rm ts}$. Using Eq.102, inserting $F_{\rm ts}$ obtained from Eq.103, then taking the average for a full period T_0 and applying $x_2\left(t\right) = A\cos\left(2\pi f_0 t\right)$ we obtain

$$\left.\frac{\triangle f}{f_0}\right|_{\rm asymm} = \frac{1}{\left(k_{\rm a} + k_{\rm c}\right) A_1^2} \frac{1}{T_0} \int_0^{T_0} \frac{nC_{\rm n} A_1 \cos\left(2\pi f_0 t\right)}{\left\{d_0 + A_1 \cos\left(2\pi f_0 t\right)\right\}^{n+1}} dt \tag{104}$$

$$= \frac{1}{2\pi} \frac{nC_{\rm n}}{\left(k_{\rm a} + k_{\rm c}\right) A D^{n+1}} \int_0^{2\pi} \frac{\cos\left(x\right)}{\left(1 + \frac{A}{D}\left(\cos\left(x\right) + 1\right)\right)^{n+1}} dx, \tag{105}$$

where we defined $A \equiv A_2$ and substituted $d_0 = D + A$ as depicted in Fig.17. D is the closest distance between tip and sample. Eq.104 can be simplified for two limiting cases:

- **Small amplitudes** $A \ll D$

  Making use of the identities $(1+\epsilon)^{-m} \approx 1 - m\epsilon$ for $\epsilon \ll 1$ and $\int_0^{2\pi} \cos^2 x dx = \pi$ yields

$$\underline{\underline{\left.\frac{\triangle f}{f_0}\right|_{\text{asymm}}} \cong -\frac{n\,(n+1)}{2\,(k_{\text{a}}+k_{\text{c}})}\frac{C_{\text{n}}}{D^{n+1}} = \frac{1}{2\,(k_{\text{a}}+k_{\text{c}})}\left.\frac{\partial^2 V_{\text{ts}}\,(z)}{\partial z^2}\right|_{z=D}}, \tag{106}$$

  which corresponds to the result of the force gradient method treated by H. Hölscher in Ref.[3].

- **Large amplitudes** $A \gg D$

  Taylor series expansion of the denominator around π and substitution $y = (A/2D)^{1/2}(x-\pi)$ yields

$$\underline{\underline{\left.\frac{\triangle f}{f_0}\right|_{\text{asymm}} \cong -\frac{1}{\sqrt{2}\pi}\frac{1}{(k_{\text{a}}+k_{\text{c}})\,A^{3/2}}\frac{nC_{\text{n}}}{D^{n+1/2}}I_1\,(n+1)}}, \tag{107}$$

  with

$$I_1\,(n+1) \equiv \int_{-\infty}^{\infty} \frac{1}{(1+y^2)^{n+1}} dy. \tag{108}$$

  Pertinent values of $I_1\,(n+1)$ are $I_1\,(2) \approx 1.6$, $I_1\,(3) \approx 1.2$, $I_1\,(4) \approx 0.98$, $I_1\,(7) \approx 0.7$, and $I_1\,(13) \approx 0.5$.

  Eq.107 can be rewritten as

$$\begin{aligned}\left.\frac{\triangle f}{f_0}\right|_{\text{asymm}} &\cong -\frac{n\,(n+1)}{2\,(k_{\text{a}}+k_{\text{c}})}\frac{C_{\text{n}}}{D^{n+1}}\cdot\frac{\sqrt{2}}{n\,(n+1)\,\pi}\left(\frac{D}{A}\right)^{3/2} I_1\,(n) \\ &= \frac{1}{2\,(k_{\text{a}}+k_{\text{c}})}\left.\frac{\partial^2 V_{\text{ts}}\,(z)}{\partial z^2}\right|_{z=D}\cdot\frac{\sqrt{2}}{n\,(n+1)\,\pi}\left(\frac{D}{A}\right)^{3/2} I_1\,(n)\,.\end{aligned} \tag{109}$$

  The first term in the relative frequency shift in Eq.109 is equal to the solution in the $A \ll D$ limit. The second term reduces the amplitude by a factor proportional $\frac{1}{n}(D/A)^{3/2}$ since $\frac{\sqrt{2}}{\pi} I_1\,(n+1) \sim 1$.

2 Bedienungsanleitung für selbstgebautes SFM HPF C17

Alle angegebenen Daten sind als Ausgangspunkte zu verstehen, mit denen das SFM sicher funktionieren wird. Durch Verändern der Parameter (v.a. der P-I-Regler) wird sicher noch eine Optimierung der Messresultate zu erzielen sein. Weitergehende Informationen sind der Diplomarbeit und dem Begleitheft zur Software der Firma Nanosurf zu entnehmen.

2.1 Vorbereitung

- Pt-Ir- oder W-Draht auf Stimmgabel mit Silber-Epoxi ankleben.
- Stimmgabel auf Stimmgabelhalter festschrauben und Füsse mit Lotandraht am Plättchen anlöten.
- Stimmgabelhalter auf Puck zum Ätzen anschrauben und auf Ätzvorrichtung einklemmen (Achtung, vergewissern, ob Kontakt zwischen Draht und Halterung vorhanden!).
- Ätzen wie in der Diplomarbeit beschrieben.

Material	Frequenz (Sinus)	Spannungsamplitude	
Pt-Ir	300Hz	bis 3V	2-Stufenverfahren
W	300Hz	bis 3V	1-Stufenverfahren

- Stimmgabelhalter von Puck zum Ätzen abschrauben, auf Puck im SFM schrauben.
- Probe einsetzen, mit x-y-Tisch positionieren.

2.2 Approach

(Grober Approach mit Mikrometerschrauben, genauer Approach mit Piezo)

- Alle Komponenten einschalten.
- Parameter auf dem Kästchen, das zwischen der Stimmgabel und der Steuerung zwischengeschaltet ist:
  - Source: Div.=1k
  - Vu=1000
  - Rcon=100k.
- Ausmessen der genauen Resonanzfrequenz der Stimmgabel:
  muss leider extern geschehen, z.B. mit dem Frequency-Analyzer.
- Notebook aufstarten und Programm "easyScan" laden:

  SFM Panel: "center frequency" eingeben, mit Multimeter kontrollieren und die abgelesene Frequenz als neue "center frequency" eingeben.
  "PLL-Gain: 0" (2mal höhere Auflösung als mit "PLL-Gain 1").
  (*nicht* "init PLL" drücken, nur "Apply")

Feedback: "Setpoint: 0.2 Hz"
"P-Gain: 7"
"I-Gain: 11"
"Feedback Loop: Stop&Clear".

- Approach Panel: noch unwichtig.
- Scan-panel öffnen
- "Befehlsleiste: Options⟶Signal Mapping...": kontrollieren, ob alle Einstellungen korrekt sind:
  - "SetPoint Sign Check: None"
  - "CtrlInput Correction: None"
  - "CtrlInput Pol: Positive"
  - "Z-Axis Polarity: Positive"
  - "ScanAxis0: Maximum 8.4252 μm"
  - "ScanAxis1: Maximum 8.4252 μm"
  - "ScanAxis2: Maximum 2.3607 μm" (Kalibrierung in Diplomarbeit)
  - "Channel0": (FrqOffset entspricht dem $\triangle f$, der Frequenzverschiebung im PLL)
    * "Maximum 183.11 Hz" (im Zusammenhang mit PLL-Gain=0)
    * "Offset": Muss jedesmal kontrolliert und eingestellt werden:
      Schliesse "Signal Mapping-Menu" (Cancel), öffne "Scan Panel" und drücke "Start", stelle den Offset im "Signal Mapping-Menu" (wieder öffnen) von Channel0 so ein, dass das Signal im FrqOffset-Fenster genau auf der eingezeichneten Linie liegt.
      (Achtung: Offset-Eichung bei "Setpoint=0 Hz" ("Feedback Panel"), erst nach Eichung "Setpoint" wieder auf 0.2 Hz stellen!).
      Danach: "Scan Panel⟶Stop" (x-y-Rasterung ausschalten).
  - "Channel1":
    * "Maximum 2.3607 μm"
    * "Offset: 0.0000 μm"
  - Am Schluss: "Ok", dann "Ja".
- PLL sollte jetzt schon angeworfen sein (vorgeschlagene Parameter für P-I-Regler: 10 kΩ und 10 μF)
- Hochspannungsverstärker einschalten, alle DC-Sources (Yokogawa) kontrollieren, ob "Output" eingeschaltet ist.
- z-Feedback in PLL einklinken: "Feedback Panel⟶Feedback Loop⟶Running".
- Spitze zurückziehen: "Approach Panel⟶Park".

- Grober Approach mit Mikrometerschrauben: die vorderen Beiden für den ganz groben Approach, die Hintere ist fünfmal feiner (Spitze-Proben-Abstand mit Mikroskop gut erkennbar).
- Feiner Approach: "Approach Panel⟶Stop".
- Vorteilhaft ist es auf dem KO die Frequenzverschiebung auf dem einen und das z-Signal auf dem anderen Kanal darzustellen. Damit kann der "Einfangvorgang" visualisiert werden.
- Falls noch nicht auf Abstand geregelt wird, muss die Spitze wieder zurückgezogen werden ("Approach Panel⟶Park"), der Aufbau behutsam heruntergeschraubt werden und die Spitze wieder heruntergelassen werden ("Approach Panel⟶Stop"). Diesen Vorgang wiederholen, bis der z-Feedback den Spitzen-Proben-Abstand regelt.
- Falls Betrieb im Vacuum: Spitze parkieren bis gewünschter Arbeitsdruck erreicht ist.

2.3 Topographie

- Voraussetzung: z-Feedback ist seit mindestens 20 Minuten am Regeln (Piezocreep).
- Wechsle im "Scan Panel" das Anzeigefenster "FrqOffset" in "ZOutput" (klicke auf Anzeigefenster "FrqOffset", öffne das "View Panel⟶Input⟶Zoutput⟶Apply").
- "Scan Panel⟶Start".
- Signal sollte möglichst genau in der Mitte des Fensters plaziert werden:
  - "Scan Panel⟶Z-Offset" einstellen: zu empfehlen ist, die automatische Regelung zu aktivieren: "Options⟶Auto Adjust Z-Offset".
  - Verkippung der Probe ausgleichen mit:
    - "Scan Panel⟶X-Slope" bei "Rotation=0.0° "
    - "Scan Panel⟶Y-Slope" bei "Rotation= 90.0°"
- Aufname eines Bildes:
  - Vorschlag für Parameter:
    - PLL: $C = 7\,\mu\text{F}$ und $R = 30\,\text{k}\Omega$
    - Feedback-Panel": P=10 und I=12
    - Scan-Geschwindigkeit: $1\,\mu$m pro Sekunde
    - für ganz schöne Bilder: "Scan Panel⟶Samples=256"
  - "Scan Panel⟶Up".
  - nach der Aufnahme: "Scan Panel⟶Photo" und dann Photo abspeichern.

2.4 "Force-Distance-Curves"

(Software noch nicht nachgebessert)

- Voraussetzung: z-Feedback ist seit mindestens 10 Minuten am Regeln (Piezocreep).
- "Feedback Panel⟶Feedback Loop⟶Stop".
- "Spectroscopy Panel" öffnen.
  - Vorschlag für Parameter
    - Averages:1
    - From: ,To: (selber rausfinden, z.B. From: -0.1 To: 0.01 (Sweep zur Probe hin))
    - (Rel. angekreuzt)
    - Time/Mod.: immer so langsam wie möglich (max: 65 s)
    - Samples: auch maximal, damit Time/Mod. vergrössert werden kann
    - Input Level:
      - Range: so gross wie die Frequenzverschiebung werden darf, z.B. 5.72 Hz
      - Offset: kommt auf die Form der "force-distance-curve" an, z.B. -0.04 Hz.
- "Spectroscopy Panel⟶Start"
- nach der Aufnahme: "Spectroscopy Panel⟶Photo" und dann Photo abspeichern.
- Die digitale Auflösung der Kurven lässt sehr zu wünschen übrig, da wir uns nur für einen Bereich von ≤ 100 nm intereressieren, aber der gesamte z-Range $\pm 2.3607\,\mu$m beträgt, d.h. wir verschenken viel Auflösung an einen Bereich, der uns nicht interessiert. Deshalb wenden wir folgenden Trick an:

  Teile die Spannung der z-Ansteuerung herunter und kalibriere den Offset manuell mit einer Gleichspannungsquelle.

  Nach dem Herunterteilen muss die Kalibrierung in

  "Options⟶Signal Mapping⟶ScanAxis2⟶Maximum"

  und "Options⟶Signal Mapping⟶Channel1 ⟶Maximum" neu eingestellt werden und zwar mit folgenden Werten:

Teilerbeschriftung:	2	$\Longrightarrow$	Maximum: 2.3607μm
	3	$\Longrightarrow$	Maximum: 0.9494μm
	4	$\Longrightarrow$	Maximum: 0.4097μm

  Weiter herunterzuteilen ist möglich, macht aber keinen Sinn.

2.5 Bemerkungen

- Alle Panels sind immer aktiv, auch wenn man sie schliesst.
- Falls man die Parameter abspeichern will: "File⟶Parameter⟶Save as"
- Falls man Bildschirmdarstellung speichern will: "File⟶Workspace⟶Save as"

Viel Glück und Geduld

Part VII
Acknowledgments

- First I'd like to thank Prof. Dr. K. Ensslin for giving me the opportunity to realize my diploma thesis.
- I'd like to thank Dr. T. Ihn for his patience and having confidence in me. He always had time for discussions and supporting me.
- Further I'd like to thank J. Rychen who shared with me his knowledge and experience of setting up and operating an SFM.
- The biggest contribution to the setup of the SFM has been done by A. Herrmann and P. Studerus who made excellent work. They had always time for discussions and prompt realization of new ideas.
- I have to thank E. Müller for the fantastic TEM-pictures of the tips and P. Wägli for the SEM-pictures.
- I'd like to thank D. Schaniel for reading and correcting this report.
- I am indepted to the entire Ensslin-team for supporting me, especially T. Vančura and R. Jäggi.

THANK YOU

References

[1] Folder "*AFM*", HPF E15, ETH Zürich.

[2] C. J. Chen, *Introduction to Scanning Tunneling Microscopy*, (Oxford University Press, New York, Oxford, 1993).

[3] H. Hölscher et al., Appl. Surf. Sci. **140** (1999) 344.

[4] H. Goldstein, *Classical Mechanics*, 2nd edn., Addison-Wesley, 1980.

[5] F. J. Giessibl, Phys. Rev. B **56**, 16010 (1997).

[6] R. J. Colton et al., *Procedures in Scanning Probe Microscopies* (Wiley, Chichester, New York, Weinheim, Brisbane, Singapore, Toronto, 1998).

[7] Th. P. Dumont, *Semesterarbeit: Elektrochemisches Ätzen von Wolfram- und Platinum/Iridium-Spitzen,* Gruppe Ensslin, ETH-Zürich, 1999.

[8] J. Rychen, personal communication.

[9] Ch. Steiner, *Semesterarbeit: Resonanzverhalten von Quarz-Stimmgabeln*, Gruppe Ensslin, ETH Zürich, 1998).

[10] Th. Ihn, personal communication.

[11] A. H. Sørensen et al., Rev. Sci. Instrum.70, 3059 (1999).

[12] F. K. Kneubühl, *Lineare und nichtlineare Schwingungen und Wellen*, (B. G. Teubner Stuttgart 1995).

[13] EBL Piezoceramic Tubes, Staveley Sensors Inc., 1994.

[14] Type GS-20DM vertical model, Geo Space Corporation, Houston Texas, U.S.A.

[15] Nanosurf AG, Austr. 4, CH-4410 Liestal, www.nanosurf.com.

[16] "epo-tek" H20E, POLYSCIENCE AG, Cham.

[17] DIN IEC 751 *Platin-Widerstandsthermometer und Messwiderstände für industrielle Anwendungen.*

[18] K. Karrai et al., Appl. Phys. Lett. **66**, 1842 (1995).

[19] J. Rychen et al., *Piezoelectric quartz tuning forks for dynamic mode scanning-probe microscopy in high magnetic fields at liquid Helium temperatures*, in preparation.

[20] W. Känzig, *Mechanik und Wellenlehre*, (vdf Verlag der Fachvereine an den schweizerischen Hochschulen und Techniken AG, Zürich 1993).

[21] N. W. Ashcroft, N. D. Mermin, *Solid State Physics*, (Saunders College Publishing, 1976).

[22] A. Sommerfeld, *Vorlesungen über theoretische Physik, Band 1 Mechanik*, (Akademische Verlagsgesellschaft Geest&Portig K.-G., Leipzig, 1962).

[23] J. N. Israelachvili, *Intermolecular and Surface Forces*, (Academic Press, 1985).

[24] J. Weis et al., *Electrostatic force between a tip electrode and a buried electrode array*, to be published.

[25] A. W. Adamson, *Physical Chemistry of Surfaces*, (3rd ed., Wiley, New York and London, 1976)

[26] F. K. Kneubühl, *Repetitorium der Physik*, (B. G. Teubner Stuttgart 1990).

[27] Goodfellow Catalogue, www.goodfellow.com.

[28] S. Belaidi et al., J. Appl. Phys. **81**, 1023 (1997).